

Analyzing and Explaining Image Classifiers via Diffusion Guidance

Maximilian Augustin

Yannic Neuhaus

Matthias Hein

Tübingen AI Center – University of Tübingen

Abstract

While deep learning has led to huge progress in complex image classification tasks like ImageNet, unexpected failure modes, e.g. via spurious features, call into question how reliably these classifiers work in the wild. Furthermore, for safety-critical tasks the black-box nature of their decisions is problematic, and explanations or at least methods which make decisions plausible are needed urgently. In this paper, we address these problems by generating images that optimize a classifier-derived objective using a framework for guided image generation. We analyze the behavior and decisions of image classifiers by visual counterfactual explanations (VCEs), detection of systematic mistakes by analyzing images where classifiers maximally disagree, and visualization of neurons to verify potential spurious features. In this way, we validate existing observations, e.g. the shape bias of adversarially robust models, as well as novel failure modes, e.g. systematic errors of zero-shot CLIP classifiers, or identify harmful spurious features. Moreover, our VCEs outperform previous work while being more versatile.

1. Introduction

Deep learning-based image classifiers suffer from several failure modes such as non-robustness to image corruptions [29, 36], spurious features and shortcuts [25, 47, 68], overconfidence on out-of-distribution inputs [28, 30, 48], adversarial examples [43, 75] or biases [24], among others.

While there has been a lot of work on detecting and measuring some of these failure modes, in our opinion, there remain two important problems that are addressed in this paper: i) systematic high-confidence predictions of classifiers, e.g. due to harmful spurious features [47], often occur on subgroups of out-of-distribution data. It is inherently difficult to find these subgroups as no data is available for them; ii) the visualization of the semantic meaning of concepts, e.g. of single neurons, or counterfactual explanations for image classifiers is extremely challenging as one has to optimize on the set of natural images and the optimization in pixel space leads to adversarial samples.

In this paper, we tackle these problems by leveraging recent progress in generative models [13, 54, 57, 60]. Our goal is to visualize properties of one or multiple image classifiers by optimizing on the approximation of the “natural image manifold” given by a latent diffusion model like Stable Diffusion [57]. This allows us to search for “unknown unknowns”, i.e. failure cases that correspond to a subpopulation of natural images which is neither easy to find in existing datasets nor allows for a textual description and is thus not amenable to direct prompting. We achieve this by using a generic framework for optimizing the inputs to a latent diffusion model to create realistic-looking images that minimize a loss function L , e.g. for the generation of images maximizing classifier disagreement, visualization of maximally activating neurons on the image manifold, and VCEs, see Fig. 1 for an overview.

Using our framework we detect systematic failure cases of a zero-shot CLIP ImageNet classifier by maximizing the difference in the predicted probability for a given class, we provide visualizations for the neurons labeled as spurious in [68] of a ResNet50 ImageNet classifier and use our technique to validate that two of them are indeed harmful spurious features [47], and finally produce realistic visual counterfactuals for any image classifier outperforming [5].

2. Related Work

Detection of systematic errors: [23] develop a pipeline to iteratively retrieve real images from LAION-5B and label failure cases where the retrieval is refined based on the labels and additional LLM captions. [39] use a 3D simulator to generate and evaluate controlled scenes containing class objects to find systematic model vulnerabilities and validate these synthetic scenes in the real world by manual reconstruction of the scenes, whereas [65] try to find transformations which leave one classifier invariant but change another classifier. [21] leverage an error-aware mixture model on a multi-modal embedding to discover systematic errors in data subsets. [14, 44, 78] use a fixed set of attributes or properties of objects to search for systematic errors for subpopulations by generating corresponding user-interpretable prompts with a fixed template structure. [12] use patch-attacks on a pixel

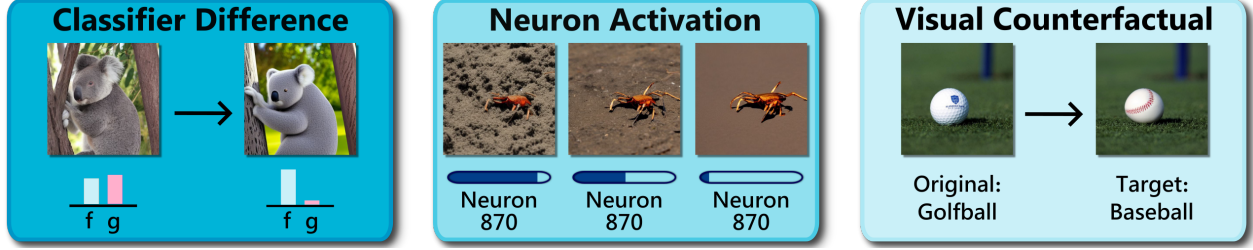


Figure 1. **Illustration of the three tasks for debugging image classifiers tackled in this paper.** **Left:** we generate images where one classifier is highly confident in a class and the other is not and recover the shape bias of adversarially robust models compared to a standard model; **Middle:** we generate images when maximizing or minimizing a neuron. We identify one neuron labeled as spurious for “fiddler crab” in [68] as associated to sand; **Right:** we produce visual counterfactual explanations for arbitrary image classifiers and outperform [5].

level or restricted attacks on the latent space of an image generator to construct perturbations which are then pasted into images. As the added patches are not coherent with the original image, the resulting image is typically unrealistic. While some of these methods use generative models to search for systematic errors this is done with a restrictive fixed search pattern. Consequently, problematic cases might be missed if they are not included in the pre-defined attribute set. In contrast, we directly optimize over the prompt/latent space and thus can find any problematic case as long as the diffusion model can generate it.

Spurious features are a particular failure mode which might be difficult to detect with fixed prompt-based or retrieval-based approaches as out-of-distribution inputs including the spurious features are confidently classified as a corresponding class, e.g. graffiti as “freight car” due to graffiti often appearing on training images of “freight car” in ImageNet [47]. [47] label a spurious feature as harmful if it can mislead the classifier to classify the image as the corresponding class without the class object being present. Most existing methods are limited to smaller datasets or subsets of ImageNet [4, 51, 66, 67], only [45, 47, 69, 70] do a full search on ImageNet. In [69], neurons of a ResNet50 were labeled as “core” or “spurious” features by inspecting Grad-Cam images and feature attacks. We show that our prompt-based optimization allows for a much easier identification of spurious features by generating realistic images that maximize or minimize the neuron activation.

Interpretability methods are often motivated by detecting failure modes of a classifier. Very popular ones are, for example, attribution methods such as GradCAM [64], Shapley values [42], Relevance Propagation [8], and LIME [56]. These methods were analyzed with mixed success regarding the detection of spurious features in [1, 2]. Counterfactual explanations [79, 80] have recently become popular but are difficult to generate for images as the optimization problem is very similar to that of adversarial examples [75]. Visual counterfactual explanations are generated via manipulation of a latent space [63], using a diffusion model [5] or in image space [6, 10, 61] for an adversarially robust classifier.

3. Method

We review diffusion models before presenting our method.

3.1. Background: Latent Diffusion Models

Score-based diffusion models [35, 71, 73] generate new samples from a data distribution $p(x)$ by progressively denoising a latent vector drawn from a prior distribution. In this work, we focus on latent diffusion models (LDMs) [57, 76] that generate new samples in the latent space of a variational auto-encoder (VAE), where \mathcal{D} denotes the de- and \mathcal{E} the corresponding encoder. We use x to denote images in pixel- and z for images in VAE-latent space. During sampling, a random latent z_T , where T corresponds to the total number of sampling steps, is drawn from the prior distribution. We then produce less and less noisy samples z_{T-1}, z_{T-2}, \dots until we reach a noise-free VAE latent z_0 , which can be transformed into pixel space using \mathcal{D} to produce the final image. The exact sequence $(z_t)_{t=0}^T$ depends on the specific solver. While diffusion models initially used stochastic samplers [35], it has been shown that one can generate high-quality samples with deterministic solvers like DDIM [72], where the entire randomness lies in the initial latent z_T . The sequence of latents $(z_t)_{t=0}^T$ for DDIM is then defined as:

$$z_{t-1} = \sqrt{\alpha_{t-1}} \frac{z_t - \sqrt{1 - \alpha_t} \epsilon(z_t, t, C)}{\sqrt{\alpha_t}} + \sqrt{1 - \alpha_{t-1}} \epsilon(z_t, t, C). \quad (1)$$

Here $(\alpha_t)_{t=1}^T$ defines the noise schedule and ϵ is the denoising model which is trained to predict the noise that was added to a noisy sample, see Appendix A for details. ϵ is typically parameterized using a U-Net [58] where an additional conditioning signal can be employed to give the user control over the outcome of the diffusion process by sampling from a conditional distribution $p(z|C)$. In this work, we use the text-to-image Stable Diffusion [57] (SD) model where the conditioning signal C is a text encoding from a CLIP [53] text encoder which is fed into the U-Net via cross-attention layers. The SD model is trained on a large set of image-text pairs [62] and covers a variety of naturally

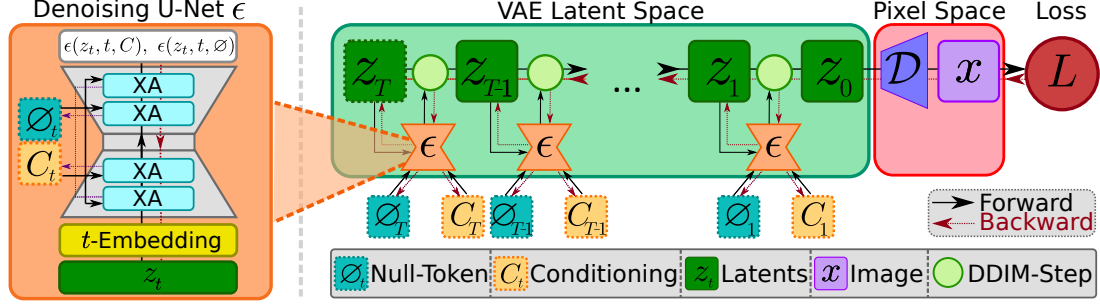


Figure 2. Illustration of the forward diffusion process (black arrows) from the initial latent z_T into the loss function L and the gradient flow during backpropagation (purple arrows). The optimization variables z_T , $(\emptyset_t)_{t=1}^T$ and $(C_t)_{t=1}^T$ are marked with a dashed border. On the left, we illustrate the conditioning mechanism inside the denoising U-Net via cross-attention (XA) layers.

occurring images. In practice, to amplify the impact of the conditioning, it is often necessary to employ classifier-free guidance [32], where $\epsilon(z_t, t, C)$ in Eq. (1) is replaced with $\hat{\epsilon}(z_t, t, C, \emptyset) = \epsilon(z_t, t, C) + w (\epsilon(z_t, t, C) - \epsilon(z_t, t, \emptyset))$, where typically $3 \leq w \leq 9$, which combines the conditional prediction $\epsilon(z_t, t, C)$ with an unconditional prediction $\epsilon(z_t, t, \emptyset)$ that is produced by replacing the conditioning vector with a null-text token \emptyset .

3.2. Optimization Framework for Visualization of Classifier Properties via Diffusion Guidance

Text-guided diffusion models have shown great success in generating highly realistic images. Several recent approaches for the detection of systematic errors leverage large text-to-image models [14, 44, 78] for the generation of images. They use fixed prompt templates describing specific properties of the desired input. However, these approaches are restricted to the variability of images encoded by their prompt templates and text guidance is often not precise enough. Our goal is an optimization framework where the image generation is directly guided by one or multiple classifiers (classifier disagreement and VCEs) or their properties (maximizing and minimizing neuron activations). Finding a text prompt that captures these tasks is just as hard as solving the task itself, *e.g.* if we want to find out what semantic concept maximizes a certain neuron we do not have access to a text description. While methods such as ControlNet [83] have shown great success at fine-grained conditioning of diffusion models, they require training samples that are not available for the tasks we want to solve and in addition, would require retraining for every vision classifier we want to explain.

However, it is easy to formulate our tasks as an optimization problem using a loss function L on the generated image. For example, we can easily calculate the activation of the target neuron from our previous example and search for highly activating images. Using the fact that the DDIM solver from the previous Section is non-stochastic, we note that the output of the entire diffusion process is a deterministic function of the initial latent z_T , the conditioning C and the null-text

token \emptyset . This allows us to formulate all our explanation tasks as optimization problems of the following form:

$$\max_{z_T, (C_t)_{t=1}^T, (\emptyset_t)_{t=1}^T} -L\left(\mathcal{D}\left(\mathbf{z}_0\left(z_T, (C_t)_{t=1}^T, (\emptyset_t)_{t=1}^T\right)\right)\right). \quad (2)$$

Here, we use $\mathbf{z}_0(z_T, (C_t)_{t=1}^T, (\emptyset_t)_{t=1}^T)$ to denote the noise-free latent which is obtained by running the diffusion process from the initial latent z_T . We also use a slightly more general form of conditioning and null-text and replace the global versions with their per-timestep counterparts $(C_t)_{t=1}^T$ and $(\emptyset_t)_{t=1}^T$ (see Figure 2). Intuitively, we search for a starting latent and conditioning that generates an image that optimizes our loss L without the need for manual prompt tuning or other forms of human supervision.

In the following Sections, we provide the corresponding loss function for each task. We want to highlight that this optimization framework is completely plug-and-play, which means that it can be used with any vision model without requiring finetuning of the generative model. In practice, storing the entire diffusion process in memory for gradient computations is not possible due to VRAM limitations and we thus use gradient checkpointing [17] to compute most of the intermediate activations as required. See Algorithm 1 for pseudo-code and more details.

4. Maximizing Classifier Disagreement

We generate maximally disagreeing images for a pair of two classifiers. This is a valuable tool to highlight differences caused by different training types, architectures, or pre-training and is particularly interesting for identifying subgroups where one classifier performs worse than the other. Forcing disagreement shifts the focus from prototypical examples of a class and makes this approach especially suitable for discovering unexpected failure modes on out-of-distribution images. Assume we are given two classifiers f, g and want to generate a realistic image that is predicted as target class y by f and not recognized by g . As objective


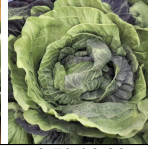
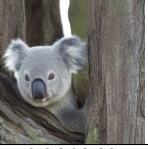


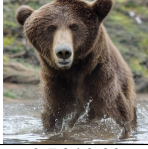





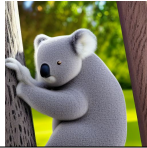


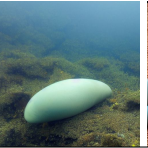
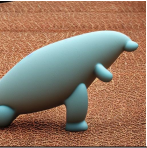
		p_f : Confidence Robust ViT-S \uparrow vs p_g : Confidence ViT-S \downarrow							
		Head Cabbage (p_f / p_g)		Koala (p_f / p_g)		Brown Bear (p_f / p_g)		Dugong (p_f / p_g)	
		0.57 / 0.95	0.70 / 0.95	0.79 / 0.96	0.76 / 0.97	0.76 / 0.96	0.67 / 0.96	0.01 / 0.01	0.14 / 0.92
SD Init.									
		0.82 / 0.00	0.79 / 0.00	0.86 / 0.00	0.92 / 0.06	0.80 / 0.00	0.76 / 0.00	0.66 / 0.02	0.78 / 0.00
$p_f \uparrow - p_g \downarrow$									

Figure 3. **Classifier disagreement: shape bias of adversarially robust models.** For a given class y , the first row shows the output of Stable Diffusion for “a photograph of y ”. The images in the second row have been optimized to maximize the confidence of an adversarially robust ViT-S while minimizing the one of a standard ViT-S. The resulting images retain the same shape but with smooth surfaces and little texture.

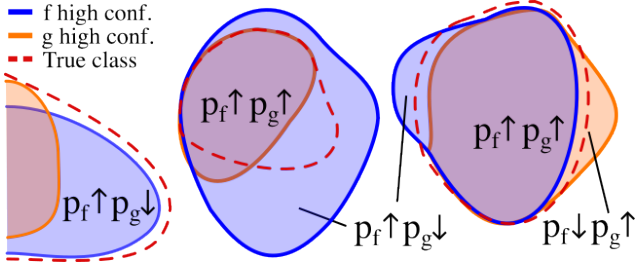


Figure 4. **Classifier Disagreement:** Images maximizing the disagreement between two classifiers f and g can reveal biases and failure modes of one or both classifiers. The three different variants we observe are: In the case of shape bias of robust models, the generated subpopulation has a schematic appearance but is still part of the true class (left). The zero-shot CLIP classifier extends the original class to a much larger set of out-of-distribution samples which causes unexpected failure modes (middle). When comparing the ViT and the ConvNext models, we find different biases by generating images inside as well as outside of the true class (right).

we use the difference of confidences in the target class y :

$$\max_{z_T, (C_t)_{t=1}^T, (\varnothing_t)_{t=1}^T} p_f(y | \mathcal{D}(z_0(z_T, (C_t)_{t=1}^T, (\varnothing_t)_{t=1}^T))) - p_g(y | \mathcal{D}(z_0(z_T, (C_t)_{t=1}^T, (\varnothing_t)_{t=1}^T))) \quad (3)$$

We initialize with a random latent and the generic prompt “a photograph of a <CLASSNAME>”.

Results: The generation of maximally disagreeing images is useful to explore subpopulations capturing classifier specific biases and failure modes. To demonstrate the versatility of this approach, we present results for three different pairs of ImageNet classifiers, exposing the shape bias of adversarially trained models, failure cases arising from the text embedding of zero-shot CLIP classifiers, and differences between ViT and ConvNeXt architectures.

Shape bias of adv. robust models: In Fig. 3 we show the difference between an adversarially trained ViT-S and

a standard ViT-S. Both variants mostly give the correct prediction with high confidence on the initial Stable Diffusion outputs. Maximizing the predicted probability of the robust model while minimizing that of the standard ViT-S, produces visible changes in the texture, e.g. smooth cartoon-like surfaces, while retaining the shapes of the objects as well as their class. The standard classifier assigns zero confidence to the generated images, whereas the confidence of the robust one increases. This verifies the shape bias of adversarially trained models which was already observed in [15, 26, 84].

Failure cases of zero-shot CLIP classifier: Next, we consider the maximally disagreeing images for an ImageNet classifier (ConvNeXt-B) and a corresponding zero-shot CLIP (ViT-B-16 trained on LAION-2B) classifier (see Fig. 5). Here, we observe several failure modes specific to the properties of the zero-shot classifier which classifies based on the cosine similarity to a text embedding of the class name. In the first two examples, an image corresponding to only parts of the class name (“waffle” for “waffle iron”, “arch bridge” for “steel arch bridge”) achieves a high similarity for the CLIP model but low confidence for the ConvNeXt. The latter is even a misclassification, as an “arch bridge” made of stone is a “viaduct” which is another ImageNet class (we further investigate this error in Fig. 12). The generated images for the classes “wooden spoon” and “space bar” show a related pattern. In these cases, the composition of individual parts of the class name achieves a high score for the CLIP model but does not resemble the intended class objects in the training set. A spoon on a wooden table is classified as “wooden spoon” and the words “space bar” in front of a “space” background are classified as “space bar”. To verify these findings, we queried the LAION-5B image retrieval API for the text embeddings of “an image of waffle”, “an image of arch bridge”, “an image of a spoon on a wooden table”, and “an image of a bar in space”. These real images produce the same results (see the second row of Fig. 5).

p_f : Confidence Zero-shot CLIP ImageNet classifier \uparrow vs. p_g : Confidence ConvNeXt-B \downarrow							
Waffle Iron (p_f / p_g)		Steel Arch Bridge (p_f / p_g)		Wooden Spoon (p_f / p_g)		Space Bar (p_f / p_g)	
1.00 / 0.01	1.00 / 0.00	1.00 / 0.00	1.00 / 0.00	0.98 / 0.00	0.92 / 0.04	1.00 / 0.00	0.99 / 0.00
							
Validation of CLIP zero-shot errors on real images from LAION-5B with retrieval query “an image of ...”							
“.. a waffle”		“.. an arch bridge”		“.. a spoon on a wooden table”		“.. a bar in space”	
1.00 / 0.18	1.00 / 0.02	0.98 / 0.00	0.99 / 0.00	0.94 / 0.00	0.99 / 0.07	0.81 / 0.00	0.40 / 0.00
							

Figure 5. **Detection of errors of the zero-shot CLIP model (ImageNet):** we generate a SD image with the prompt “a photograph of <CLASSNAME>”. Starting from this image, we maximize the difference between the predicted probability for the target class of a zero-shot CLIP ImageNet model and a ConvNeXt-B trained on ImageNet (first row). We find subpopulations of images that are systematically misclassified by the CLIP model: waffles are classified as “waffle iron”, stone briges as “steel arch bridges”, spoons on a wooden table as “wooden spoon”, and images with space and bar as “space bar”. In the second row we validate these errors by finding similar real images in LAION-5B (see App. B). The errors of CLIP are most likely an artefact of the text embeddings due to the composition of the class name.

Comparing biases: ViT vs ConvNeXt: We investigate the differences between a ViT-B and a ConvNeXt-B. We generate two images by maximizing the confidence of one while minimizing the other and vice versa (see Fig. 23 in App. D). We discover subtle biases when maximizing the confidence of the ConvNeXt for “goblet”: empty wine glasses are generated and classified confidently as “goblet” by the ConvNeXt and “red wine” by the ViT. Both of them are wrong, as the image is not from the ImageNet classes. Nevertheless, insights about this kind of consistent behavior on out-of-distribution samples can help to detect failure modes that would occur after the release of the model and cannot be noticed by inspecting the training or test dataset. More details in App. D.

5. Neuron Activation

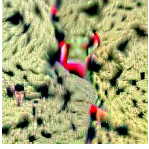

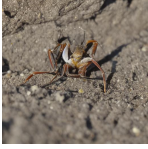

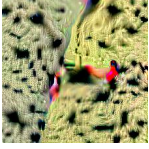


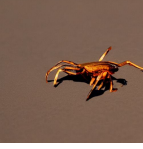
In the next task, we want to visualize the semantic meaning of specific neurons in the last layer of a classification model. While the neurons in earlier layers of DNNs and convolutional NNs in particular, are thought to capture low-level image features like corners and edges, neurons in the last layer are meant to capture more semantically meaningful concepts [20]. For this task, assume we are given a classifier f and let $\phi : \mathbb{R}^D \rightarrow \mathbb{R}^N$ denote the function that maps an input image into its feature representation at the final layer before the linear classification head. Assume we are also given a target neuron $n \in \{1, \dots, N\}$ and class y . Our objective is to maximize the activation of that neuron starting from a random latent and the same generic prompt as in the previous task using the loss:

$$\max_{z_T, (C_t)_{t=1}^T, (\emptyset_t)_{t=1}^T} \phi \left(\mathcal{D} \left(\mathbf{z}_0 \left(z_T, (C_t)_{t=1}^T, (\emptyset_t)_{t=1}^T \right) \right) \right)_n \cdot (4)$$

Similarly, it can also be helpful to minimize the activation of a specific neuron, for which we simply minimize its activation instead of maximizing it. So far a common way to identify the concepts captured by individual neurons is to inspect maximizing and minimizing training images. However, such subpopulations in real data usually differ in many aspects which makes this analysis ambiguous. In contrast, generated images optimized to increase or decrease the activation of a neuron improve interpretability as many parts of the initial images remain unchanged and thus changes associated with the neuron can be easily identified.

Results: Generated images that maximize individual neurons have been used to detect spurious features [68]. In Fig. 6, we compare our approach to their “Feature attack” starting from the same initial image (generated with Stable Diffusion). Their procedure achieves a higher neuron activation but the resulting images lack realism as they show mostly artificial patterns. In addition, they mostly reduce the confidence in the spuriously correlated class. On the other hand, our results convey a clearer interpretation of the corresponding semantic concept: Maximizing the neurons amplifies the presence of the corresponding spurious concepts (“sand” for “fiddler crab” and “dry gras” for “prairie chicken”), whereas minimizing removes them completely. In both examples, the main objects are only changed minimally compared to the initial SD image. Also, the confidence for the spuriously correlated class increases even though the class object is partially hidden by the “sand” or “grass”. This strongly suggests that both of them are cases of harmful spurious features, i.e. their presence in images that do not contain the actual class already triggers the prediction of the

Neuron 870 (Conf. class Fiddler crab)

[68] Max. Neuron 870	Maximize Neuron 870	← SD → Initialization	Minimize Neuron 870
11.16 (0.00)	2.74 (0.92)	1.76 (0.72)	0.24 (0.00)
			
11.18 (0.00)	2.67 (0.97)	1.19 (0.64)	0.25 (0.08)
			

Neuron 565 (Conf. class Prairie chicken)


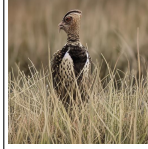
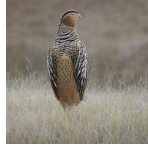
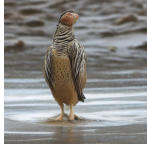

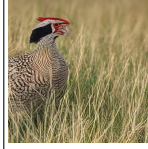
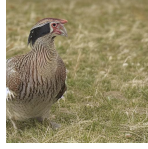
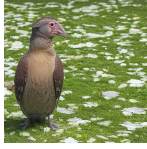
[68] Max. Neuron 565	Maximize Neuron 565	← SD → Initialization	Minimize Neuron 565
16.42 (0.66)	3.82 (0.61)	1.91 (0.59)	0.52 (0.01)
			
16.02 (0.38)	3.23 (0.88)	1.41 (0.59)	0.26 (0.00)
			

Figure 6. **Neuron visualizations for spurious feature detection:** We visualize neurons marked as spurious for a specific class in [68]. Starting from the output of Stable Diffusion for “an image of <class name>”, we maximize and minimize the value of the corresponding spurious neuron. On the left we show the result of the feature attack maximizing the neuron of [68] for comparison. Our resulting images convey the semantic meaning of the neuron, whereas the feature attack is too extreme. For the class “fiddler crab”, maximizing the spurious neuron enhances the sandy background in the image, whereas minimizing the neuron removes the sand completely. Similarly, the semantic feature “dry gras” is amplified or removed in the “prairie chicken” images when the spurious neuron is maximized or minimized, respectively.









	Neuron 870 (Conf. class Fiddler crab)		Neuron 565 (Conf. class Prairie chicken)	
	House Finch	Bee	Hartebeest	Bull frog
	0.26 (0.00)	0.76 (0.00)	1.09 (0.00)	0.58 (0.00)
SD Init.				
	1.62 (0.46)	2.12 (0.51)	3.87 (0.27)	2.88 (0.85)
Max. Neuron				

Figure 7. **Validating two harmful spurious features:** Maximizing the spurious neuron 870 of class “fidler crab” starting from different classes “house finch” and “bee”, only sand appears on images of a bird and a bee. Nevertheless the classifier predicts confidently “fiddler crab” which show that neuron 870 is a harmful spurious feature, i.e. it triggers the prediction although the class object is not in the image [47]. The same observation is true for neuron 565.

class [47]. We test this in Fig. 7 where we start from the image of a *different* class. Our method produces images of a bird and a bee surrounded by sand which are still classified as “fiddler crab” or a hartebeest and a frog behind dry grass which are classified as “prairie chicken”. Using our method, we even uncover errors in the labeling of the neurons: Due to the inconclusive visualizations in [68], neuron 1678 has been marked as “spurious” for class “microphone” by three out of five human labelers. However, our images confirm that it actually corresponds to the head of the microphone and is therefore a “core” feature of that class (see Fig. 8).

Neuron 1678 (Conf. class Microphone)







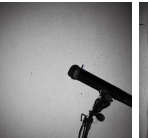

[68] Max. Neuron 1678	Maximize Neuron 1678	← SD → Initialization	Minimize Neuron 1678
14.22 (0.92)	1.27 (1.00)	0.29 (0.97)	0.00 (0.14)
			
14.37 (0.00)	1.36 (1.00)	0.86 (0.09)	0.16 (0.01)
			

Figure 8. **Revealing label error:** in [68] neuron 1678 was marked as spurious by 3 out of 5 labelers due to ambiguous visualization. Our method shows that this neuron corresponds to the head of the microphone which is “core”, not “spurious”. Maximizing the neuron yields a more detailed head, minimizing removes the head.

6. Visual Counterfactual Explanations

Counterfactual reasoning has become a valuable tool for understanding the behavior of models. For image classifiers, a Visual Counterfactual Explanation (VCE) [5, 10] for input \hat{x} , target class y and classifier f is a new image x , that **i)** is classified as y by f (actionable), **ii)** looks realistic (on the natural image manifold), **iii)** contains minimal changes to the input \hat{x} . In particular, that the VCE x is actionable distinguishes it from other explanation techniques. Prior methods that generate VCEs for ImageNet require an additional dataset-specific adversarially robust model [5]. In contrast, our method is training-free and produces VCEs for *any* classifier trained

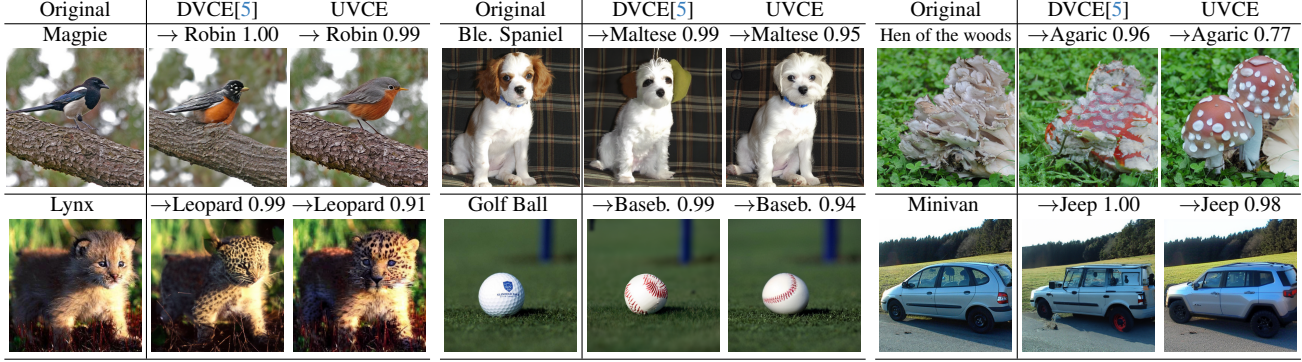


Figure 9. **ImageNet VCEs:** We show the original ImageNet validation image as well as DVCE[5] and our UVCE with the corresponding confidence in the target class. Our UVCEs are more realistic looking and are able to produce fine-grained texture changes ("leopard", "baseball") as well as more complex geometric transformations ("agaric", "jeep") where DVCE often fails to create a coherent object.

on *any* dataset containing natural images. We thus refer to our generated counterfactuals as *Universal VCE (UVCE)*.

VCE generation is a challenging image-to-image task. The loss for VCE generation has to include a similarity measure to the original image in addition to the predicted probability of f in class y . As the optimization problem is highly non-convex, we need a good initialization for better performance and convergence. We describe our method in the following (see Appendix C for pseudo-code and a visualization of the individual steps).

VCE Initialization: As the VCE should be similar to the original image, random initialization is suboptimal. In order to find a latent z_T that reproduces the image \hat{x} , we use Null-Text inversion [46] which, on top of the latent z_T optimizes a per-time step null-token $(\emptyset_t)_{t=1}^T$ to improve reconstruction. As the inversion is dependent on the text conditioning and we want a fully automated pipeline, we need a text description \hat{P} of \hat{x} . We use Open-Flamingo [3, 7] to extend the generic caption "an image of a <ORIGINAL CLASSNAME>" with additional details and then decode this caption using the CLIP encoder in SD to get an initial conditioning \hat{C} . By doing so, we can find $(z_T, \hat{C}, (\emptyset_t)_{t=1}^T)$ that closely reconstruct the original image. In order to get an even better initialization, we make use of the extensive knowledge contained in SD. We replace the original class name with the name of the target class in the prompt \hat{P} to get a modified prompt P , so "an image of a dog at the beach" becomes "an image of a cat at the beach". This prompt can be decoded into a new conditioning C that contains the target class. Due to the change from \hat{C} to C , reconstructing the image with the new conditioning C yields images with different overall structure. We thus use a modified version of Prompt-to-Prompt from [31], who found that one can preserve structure by injecting cross-attention (XA) maps. This style of editing often results in a good initialization, but several issues prevent it from being a VCE method on its own. Most importantly, as f is not involved, the resulting images often have low confidence

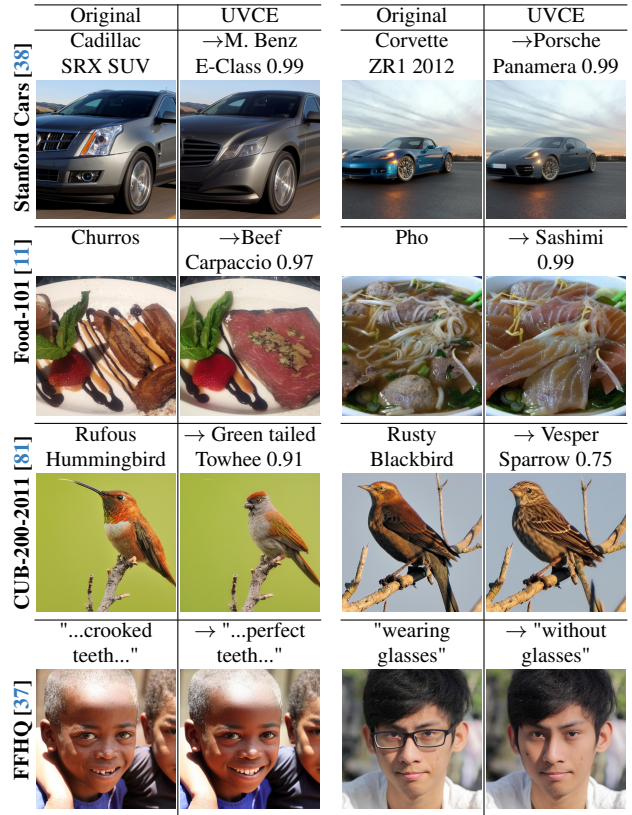


Figure 10. **VCEs for various datasets.** UVCE is the first training-free method that can generate highly realistic VCEs for any dataset containing natural images without requiring a dataset-specific generative model or an adversarially robust classifier.

and secondly, it induces more changes than necessary, see Figure 11. To overcome those issues, we propose to jointly optimize the confidence and distance to the starting image.

VCE Optimization: To ensure the similarity of the VCE x to the starting image \hat{x} , we would ideally like to change the class object while keeping the background the same. Prior works [5, 10] use L_p regularization between x and \hat{x} to keep

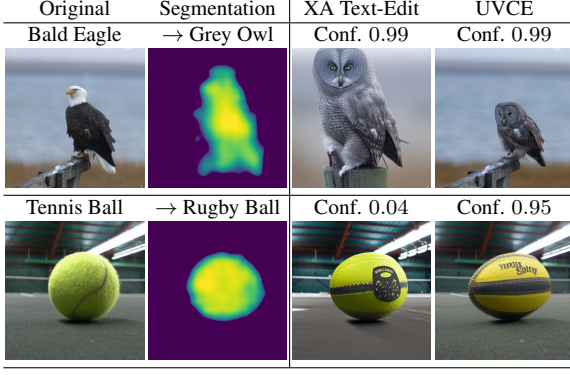


Figure 11. **Comparison of UVCEs to text-guided changes with XA injection that we use as initialization:** We show examples where the P2P-style initialization fails. It yields either unnecessarily large background changes and/or does not yield images with high confidence into the target class. In all cases, our optimization is able to both restore the background as well as increase the confidence into the target class by creating the proper class object.

the changes minimal. However, L_p distances between images depend heavily on the size of the foreground object. If the class object is small, we only want to allow minimal changes in the image, while for larger class objects we need to allow larger changes. As the XA maps encode the locations that are most influenced by a specific text token, we can use them to compute soft segmentation masks in the VAE latent (S_{VAE}) and pixel space (S_{PX}), where $S_{i,j} \approx 1$ if location (i, j) corresponds to the foreground object. Given these segmentations, we define our foreground aware distance term that penalizes background changes to the original image \hat{x} and its VAE encoding $\mathcal{E}(\hat{x})$ while simultaneously allowing for large changes in color and shape in the foreground:

$$d(z, \hat{x}) = w_{VAE} \|(1 - S_{VAE}) \odot (z - \mathcal{E}(\hat{x}))\|_2^2 + w_{PX} \|(1 - S_{PX}) \odot (\mathcal{D}(z) - \hat{x})\|_2^2. \quad (5)$$

The final loss for the VCE generation is then given by:

$$\max_{z_T, (C_t)_{t=1}^T, (\emptyset_t)_{t=1}^T} -d\left(\mathbf{z}_0(z_T, (C_t)_{t=1}^T, (\emptyset_t)_{t=1}^T), \hat{x}\right) + \log p_f\left(y | \mathcal{D}(\mathbf{z}_0(z_T, (C_t)_{t=1}^T, (\emptyset_t)_{t=1}^T))\right). \quad (6)$$

Evaluation: We compare our UVCE to DVCEs [5] which is the most recent VCE method that works on ImageNet. We emphasize that, unlike DVCEs, we do not require a robust classifier or a dataset-specific diffusion model. We generate counterfactuals into classes that are close in the ImageNet hierarchy and show qualitative results in Fig. 9. While DVCEs work well for some images, they often produce unrealistic results. For example, for “Agaric” or “Jeep”, DVCEs contain some features of the target class but the method fails to create a coherent object. In other cases, some parts of the generated

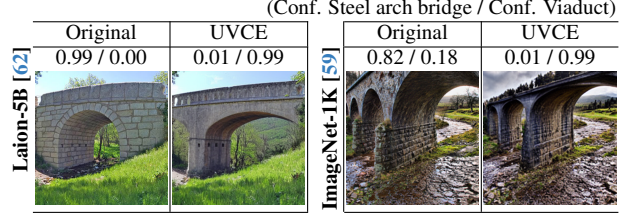


Figure 12. **Revisiting zero-shot CLIP error via UVCE:** 14% of the ImageNet validation images of class “viaduct” are misclassified as “steel arch bridge” by the CLIP zero-shot model (error detected in Fig. 5). We generate UVCEs for **wrongly** classified images and with the correct class “viaduct” as target. We find that the classifier distinguishes the two classes based on the shape of the arch. This shows that the CLIP model has learned a wrong decision boundary and how UVCEs can be used to understand systematic misclassifications, in this case narrow stone bridges are classified as “steel arch bridge” although they should be classified as “viaduct”.

class seem artificial or illogical like the ear of the dog and the stitches on the baseball. In contrast, our approach consistently produces more realistic changes into the target class. To validate our method, we did a user study on randomly selected images where we asked the participants to rate if “the counterfactual image ” **Q1** “... is realistic” **Q2** “... shows meaningful features of the target class” **Q3** “... changes mainly the class object”. We also asked the participants to directly rate whether the DVCE or the UVCE counterfactual is better or if both are equal. Results are in Table 1 and further details and the images of the study are in Appendix F. Users rated our UVCE as more realistic and as better showing the features of the target class. Our UVCEs were preferred over DVCEs in 62.8% of cases, 16.2% preferred DVCEs and 22% rated both equal.

	Q1	Q2	Q3	Better?
DVCE[5]	35.8%	59.6%	76.1%	16.2 %
UVCE	77.1%	81.1%	78.3%	62.8%

Table 1. **User Study.** Our UVCEs are rated as more realistic (Q1), showing better features of the target class (Q2), and overall better.

We emphasize that, unlike previous approaches like DVCE, we can generate our UVCEs for *any* image classifier (no robustness or specific diffusion model required) on *any* natural image dataset and we show examples for Cars, CUB, and Food as well as zero-shot attribute classification on FFHQ in Fig. 10 and additional examples in Appendix C. In addition, Fig. 12 contains an error analysis of CLIP using UVCE where we visualize what a *wrongly* predicted image would have to look like to be correctly classified.

7. Conclusion and Limitations

In this work, we have introduced a framework for analyzing and explaining *any* differentiable image classifier via dif-

fusion guidance. We demonstrated that it enables flexible detection of systematic biases on in- and out-of-distribution data. Additionally, our work improves the understanding of classifier decisions by creating realistic and interpretable visualizations of individual neurons as well as better and more universal visual counterfactual explanations.

Limitations. Blind spots of the diffusion model can be inherited which prevents the detection of these subgroups.

Acknowledgements

We are grateful for support by the DFG, Project number 390727645, and the Carl Zeiss Foundation, project “Certification and Foundations of Safe Machine Learning Systems in Healthcare”. The authors thank the IMPRS-IS for supporting YN.

References

- [1] Julius Adebayo, Michael Muelly, Hal Abelson, and Been Kim. Post hoc explanations may be ineffective for detecting unknown spurious correlation. In *ICLR*, 2022. 2
- [2] Julius Adebayo, Michael Muelly, Iaria Liccardi, and Been Kim. Debugging tests for model explanations. In *NeurIPS*, 2020. 2
- [3] Jean-Baptiste Alayrac, Jeff Donahue, Pauline Luc, Antoine Miech, Iain Barr, Yana Hasson, Karel Lenc, Arthur Mensch, Katie Millican, Malcolm Reynolds, Roman Ring, Eliza Rutherford, Serkan Cabi, Tengda Han, Zhitao Gong, Sina Samangooei, Marianne Monteiro, Jacob Menick, Sebastian Borgeaud, Andy Brock, Aida Nematzadeh, Sahand Sharifzadeh, Mikolaj Binkowski, Ricardo Barreira, Oriol Vinyals, Andrew Zisserman, and Karen Simonyan. Flamingo: a visual language model for few-shot learning. In *NeurIPS*, 2022. 7, 15
- [4] Christopher J. Anders, Leander Weber, David Neumann, Wojciech Samek, Klaus-Robert Müller, and Sebastian Lapuschkin. Finding and removing clever hans: Using explanation methods to debug and improve deep models. *Information Fusion*, 77:261–295, 2022. 2
- [5] Maximilian Augustin, Valentyn Boreiko, Francesco Croce, and Matthias Hein. Diffusion visual counterfactual explanations. In *NeurIPS*, 2022. 1, 2, 6, 7, 8, 12, 20, 21
- [6] Maximilian Augustin, Alexander Meinke, and Matthias Hein. Adversarial robustness on in- and out-distribution improves explainability. In *ECCV*, 2020. 2, 15
- [7] Anas Awadalla, Irena Gao, Josh Gardner, Jack Hessel, Yusuf Hanafy, Wanrong Zhu, Kalyani Marathe, Yonatan Bitton, Samir Gadre, Shiori Sagawa, Jenia Jitsev, Simon Kornblith, Pang Wei Koh, Gabriel Ilharco, Mitchell Wortsman, and Ludwig Schmidt. Openflamingo: An open-source framework for training large autoregressive vision-language models. *arXiv preprint arXiv:2308.01390*, 2023. 7, 15
- [8] David Baehrens, Timon Schroeter, Stefan Harmeling, Motoaki Kawanabe, Katja Hansen, and Klaus-Robert Müller. How to explain individual classification decisions. *JMLR*, 2010. 2
- [9] Arpit Bansal, Hong-Min Chu, Avi Schwarzschild, Soumyadip Sengupta, Micah Goldblum, Jonas Geiping, and Tom Goldstein. Universal guidance for diffusion models. *arXiv preprint arXiv:2302.07121*, 2023. 13
- [10] Valentyn Boreiko, Maximilian Augustin, Francesco Croce, Philipp Berens, and Matthias Hein. Sparse visual counterfactual explanations in image space. In *GCPR*, 2022. 2, 6, 7
- [11] Lukas Bossard, Matthieu Guillaumin, and Luc Van Gool. Food-101 – mining discriminative components with random forests. In *ECCV*, 2014. 7, 22
- [12] Stephen Casper, Max Nadeau, Dylan Hadfield-Menell, and Gabriel Kreiman. Robust feature-level adversaries are interpretability tools. In *NeurIPS*, 2022. 1
- [13] Huiwen Chang, Han Zhang, Jarred Barber, AJ Maschinot, Jose Lezama, Lu Jiang, Ming-Hsuan Yang, Kevin Murphy, William T Freeman, Michael Rubinstein, et al. Muse: Text-to-image generation via masked generative transformers. *arXiv preprint arXiv:2301.00704*, 2023. 1
- [14] Muxi Chen, Yu Li, and Qiang Xu. Hibus: On human-interpretable model debug. In *NeurIPS*, 2023. 1, 3
- [15] Peijie Chen, Chirag Agarwal, and Anh Nguyen. The shape and simplicity biases of adversarially robust imagenet-trained cnns. *arXiv preprint arXiv:2006.09373*, 2020. 4
- [16] Ricky TQ Chen, Yulia Rubanova, Jesse Bettencourt, and David K Duvenaud. Neural ordinary differential equations. *NeurIPS*, 2018. 13
- [17] Tianqi Chen, Bing Xu, Chiyuan Zhang, and Carlos Guestrin. Training deep nets with sublinear memory cost. *arXiv preprint arXiv:1604.06174*, 2016. 3
- [18] Prafulla Dhariwal and Alex Nichol. Diffusion models beat gans on image synthesis. In *NeurIPS*, 2021. 13
- [19] Alexey Dosovitskiy, Lucas Beyer, Alexander Kolesnikov, Dirk Weissenborn, Xiaohua Zhai, Thomas Unterthiner, Mostafa Dehghani, Matthias Minderer, Georg Heigold, Sylvain Gelly, et al. An image is worth 16x16 words: Transformers for image recognition at scale. *ICLR*, 2021. 13, 21, 22
- [20] Logan Engstrom, Andrew Ilyas, Shibani Santurkar, Dimitris Tsipras, Brandon Tran, and Aleksander Madry. Adversarial robustness as a prior for learned representations, 2019. 5
- [21] Sabri Eyuboglu, Maya Varma, Khaled Saab, Jean-Benoit Delbrouck, Christopher Lee-Messer, Jared Dunnmon, James Zou, and Christopher Ré. Domino: Discovering systematic errors with cross-modal embeddings. In *ICLR*, 2022. 1
- [22] Samir Yitzhak Gadre, Gabriel Ilharco, Alex Fang, Jonathan Hayase, Georgios Smyrnis, Thao Nguyen, Ryan Marten, Mitchell Wortsman, Dhruva Ghosh, Jieyu Zhang, et al. Data-comp: In search of the next generation of multimodal datasets. *arXiv preprint arXiv:2304.14108*, 2023. 20
- [23] Irena Gao, Gabriel Ilharco, Scott Lundberg, and Marco Tulio Ribeiro. Adaptive testing of computer vision models. In *ICCV*, 2023. 1
- [24] R. Geirhos, P. Rubisch, C. Michaelis, M. Bethge, F. A. Wichmann, and W. Brendel. Imagenet-trained cnns are biased towards texture; increasing shape bias improves accuracy and robustness. In *ICLR*, 2019. 1

- [25] Robert Geirhos, Jörn-Henrik Jacobsen, Claudio Michaelis, Richard Zemel, Wieland Brendel, Matthias Bethge, and Felix A. Wichmann. Shortcut learning in deep neural networks. *Nature Machine Intelligence*, 2(11):665–673, 2020. 1
- [26] Robert Geirhos, Kantharaju Narayanappa, Benjamin Mitzkus, Tizian Thieringer, Matthias Bethge, Felix A. Wichmann, and Wieland Brendel. Partial success in closing the gap between human and machine vision. *NeurIPS*, 2021. 4
- [27] Kaiming He, Xinlei Chen, Saining Xie, Yanghao Li, Piotr Dollár, and Ross Girshick. Masked autoencoders are scalable vision learners. In *CVPR*, 2022. 20, 22
- [28] M. Hein, M. Andriushchenko, and J. Bitterwolf. Why ReLU networks yield high-confidence predictions far away from the training data and how to mitigate the problem. In *CVPR*, 2019. 1
- [29] D. Hendrycks and T. Dietterich. Benchmarking neural network robustness to common corruptions and perturbations. In *ICLR*, 2019. 1
- [30] D. Hendrycks and K. Gimpel. A baseline for detecting misclassified and out-of-distribution examples in neural networks. In *ICLR*, 2017. 1
- [31] Amir Hertz, Ron Mokady, Jay Tenenbaum, Kfir Aberman, Yael Pritch, and Daniel Cohen-Or. Prompt-to-prompt image editing with cross attention control. *arXiv preprint arXiv:2208.01626*, 2022. 7, 18, 19
- [32] Jonathan Ho and Tim Salimans. Classifier-free diffusion guidance. In *NeurIPS Workshop*, 2021. 3
- [33] Jonathan Ho and Tim Salimans. Classifier-free diffusion guidance. *arXiv preprint arXiv:2207.12598*, 2022. 13
- [34] Gabriel Ilharco, Mitchell Wortsman, Ross Wightman, Cade Gordon, Nicholas Carlini, Rohan Taori, Achal Dave, Vaishaal Shankar, Hongseok Namkoong, John Miller, Hannaneh Hajishirzi, Ali Farhadi, and Ludwig Schmidt. Openclip, July 2021. 20
- [35] Pieter Abbeel Jonathan Ho, Ajay Jain. Denoising diffusion probabilistic models. In *NeurIPS*, 2020. 2, 12, 13
- [36] Oğuzhan Fatih Kar, Teresa Yeo, Andrei Atanov, and Amir Zamir. 3d common corruptions and data augmentation. In *CVPR*, 2022. 1
- [37] Tero Karras, Samuli Laine, Miika Aittala, Janne Hellsten, Jaakko Lehtinen, and Timo Aila. Analyzing and improving the image quality of StyleGAN. In *CVPR*, 2020. 7, 20
- [38] Jonathan Krause, Michael Stark, Jia Deng, and Li Fei-Fei. 3d object representations for fine-grained categorization. In *Proceedings of the IEEE international conference on computer vision workshops*, 2013. 7, 23
- [39] Guillaume Leclerc, Hadi Salman, Andrew Ilyas, Sai Vemprala, Logan Engstrom, Vibhav Vineet, Kai Xiao, Pengchuan Zhang, Shibani Santurkar, Greg Yang, Ashish Kapoor, and Aleksander Madry. 3db: A framework for debugging computer vision models. In *NeurIPS*, 2022. 1
- [40] Wei Li, Xue Xu, Xinyan Xiao, Jiachen Liu, Hu Yang, Guohao Li, Zhanpeng Wang, Zhifan Feng, Qiaoqiao She, Yajuan Lyu, et al. Upainting: Unified text-to-image diffusion generation with cross-modal guidance. *arXiv preprint arXiv:2210.16031*, 2022. 13
- [41] Xianhang Li, Zeyu Wang, and Cihang Xie. An inverse scaling law for clip training. In *NeurIPS*, 2023. 20, 23
- [42] Scott M. Lundberg and Su-In Lee. A unified approach to interpreting model predictions. In *NeurIPS*, 2017. 2
- [43] Aleksander Madry, Aleksandar Makelov, Ludwig Schmidt, Dimitris Tsipras, and Adrian Vladu. Towards deep learning models resistant to adversarial attacks. In *ICLR*, 2018. 1
- [44] Jan Hendrik Metzen, Robin Huttmacher, N. Grace Hua, Valentyn Boreiko, and Dan Zhang. Identification of systematic errors of image classifiers on rare subgroups. In *ICCV*, 2023. 1, 3
- [45] Mazda Moayeri, Sahil Singla, and Soheil Feizi. Hard ImageNet: Segmentations for objects with strong spurious cues. In *NeurIPS Datasets and Benchmarks Track*, 2022. 2
- [46] Ron Mokady, Amir Hertz, Kfir Aberman, Yael Pritch, and Daniel Cohen-Or. Null-text inversion for editing real images using guided diffusion models. *arXiv preprint arXiv:2211.09794*, 2022. 7, 14, 17
- [47] Yannic Neuhaus, Maximilian Augustin, Valentyn Boreiko, and Matthias Hein. Spurious features everywhere – large-scale detection of harmful spurious features in imagenet, 2023. 1, 2, 6
- [48] A. Nguyen, J. Yosinski, and J. Clune. Deep neural networks are easily fooled: High confidence predictions for unrecognizable images. In *CVPR*, 2015. 1
- [49] Alex Nichol, Prafulla Dhariwal, Aditya Ramesh, Pranav Shyam, Pamela Mishkin, Bob McGrew, Ilya Sutskever, and Mark Chen. Glide: Towards photorealistic image generation and editing with text-guided diffusion models. In *ICML*, 2022. 13
- [50] Weili Nie, Brandon Guo, Yujia Huang, Chaowei Xiao, Arash Vahdat, and Anima Anandkumar. Diffusion models for adversarial purification. In *ICML*, 2022. 15
- [51] Gregory Plumb, Marco Tulio Ribeiro, and Ameet Talwalkar. Finding and fixing spurious patterns with explanations. *Transactions on Machine Learning Research (TMLR)*, 2022. 2
- [52] Alec Radford, Jong Wook Kim, Chris Hallacy, Aditya Ramesh, Gabriel Goh, Sandhini Agarwal, Girish Sastry, Amanda Askell, Pamela Mishkin, Jack Clark, et al. Learning transferable visual models from natural language supervision. In *ICML*, 2021. 13
- [53] Alec Radford, Jong Wook Kim, Chris Hallacy, Aditya Ramesh, Gabriel Goh, Sandhini Agarwal, Girish Sastry, Amanda Askell, Pamela Mishkin, Jack Clark, Gretchen Krueger, and Ilya Sutskever. Learning transferable visual models from natural language supervision. In *ICML*, 2021. 2
- [54] Aditya Ramesh, Prafulla Dhariwal, Alex Nichol, Casey Chu, and Mark Chen. Hierarchical text-conditional image generation with clip latents. *arXiv preprint arXiv:2204.06125*, 2022. 1
- [55] Yongming Rao, Guangyi Chen, Jiwen Lu, and Jie Zhou. Counterfactual attention learning for fine-grained visual categorization and re-identification. In *ICCV*, 2021. 20, 23
- [56] Marco Tulio Ribeiro, Sameer Singh, and Carlos Guestrin. "why should i trust you?": Explaining the predictions of any classifier. In *KDD*, 2016. 2
- [57] Robin Rombach, Andreas Blattmann, Dominik Lorenz, Patrick Esser, and Björn Ommer. High-resolution image synthesis with latent diffusion models. In *CVPR*, 2022. 1, 2, 12, 13

- [58] Olaf Ronneberger, Philipp Fischer, and Thomas Brox. U-net: Convolutional networks for biomedical image segmentation. In *MICCAI*, 2015. 2, 14
- [59] Olga Russakovsky, Jia Deng, Hao Su, Jonathan Krause, Sanjeev Satheesh, Sean Ma, Zhiheng Huang, Andrej Karpathy, Aditya Khosla, Michael Bernstein, et al. Imagenet large scale visual recognition challenge. *IJCV*, 2015. 8, 21
- [60] Chitwan Saharia, William Chan, Saurabh Saxena, Lala Li, Jay Whang, Emily L Denton, Kamyar Ghasemipour, Raphael Gontijo Lopes, Burcu Karagol Ayan, Tim Salimans, et al. Photorealistic text-to-image diffusion models with deep language understanding. *NeurIPS*, 2022. 1, 13
- [61] Shibani Santurkar, Dimitris Tsipras, Brandon Tran, Andrew Ilyas, Logan Engstrom, and Aleksander Madry. Image synthesis with a single (robust) classifier. In *NeurIPS*, 2019. 2
- [62] Christoph Schuhmann, Romain Beaumont, Richard Vencu, Cade Gordon, Ross Wightman, Mehdi Cherti, Theo Coombes, Aarush Katta, Clayton Mullis, Mitchell Wortsman, et al. Laion-5b: An open large-scale dataset for training next generation image-text models. *arXiv preprint arXiv:2210.08402*, 2022. 2, 8
- [63] Kathryn Schutte, Olivier Moindrot, Paul Hérent, Jean-Baptiste Schiratti, and Simon Jégou. Using stylegan for visual interpretability of deep learning models on medical images. In *NeurIPS Workshop*, 2020. 2
- [64] Ramprasaath R. Selvaraju, Michael Cogswell, Abhishek Das, Ramakrishna Vedantam, Devi Parikh, and Dhruv Batra. Grad-cam: Visual explanations from deep networks via gradient-based localization. In *ICCV*, 2017. 2
- [65] Harshay Shah, Sung Min Park, Andrew Ilyas, and Aleksander Madry. ModelDiff: A framework for comparing learning algorithms. In *ICML*, volume 202. PMLR, 2023. 1
- [66] Rakshith Shetty, Bernt Schiele, and Mario Fritz. Not using the car to see the sidewalk—quantifying and controlling the effects of context in classification and segmentation. In *CVPR*, 2019. 2
- [67] Krishna Kumar Singh, Dhruv Mahajan, Kristen Grauman, Yong Jae Lee, Matt Feiszli, and Deepti Ghadiyaram. Don’t judge an object by its context: learning to overcome contextual bias. In *CVPR*, 2020. 2
- [68] Sahil Singla and Soheil Feizi. Salient imagenet: How to discover spurious features in deep learning? In *ICLR*, 2022. 1, 2, 5, 6, 12, 24, 27
- [69] Sahil Singla and Soheil Feizi. Salient imagenet: How to discover spurious features in deep learning? In *ICLR*, 2022. 2
- [70] Sahil Singla, Mazda Moayeri, and Soheil Feizi. Core risk minimization using salient imagenet. *arXiv:2203.15566*, 2022. 2
- [71] Jascha Sohl-Dickstein, Eric Weiss, Niru Maheswaranathan, and Surya Ganguli. Deep unsupervised learning using nonequilibrium thermodynamics. In *ICML*, 2015. 2, 12, 13
- [72] Jiaming Song, Chenlin Meng, and Stefano Ermon. Denoising diffusion implicit models. In *ICLR*, 2021. 2, 12, 13, 17
- [73] Yang Song, Jascha Sohl-Dickstein, Diederik P Kingma, Abhishek Kumar, Stefano Ermon, and Ben Poole. Score-based generative modeling through stochastic differential equations. In *ICLR*, 2021. 2, 12, 13
- [74] Andreas Steiner, Alexander Kolesnikov, Xiaohua Zhai, Ross Wightman, Jakob Uszkoreit, and Lucas Beyer. How to train your vit? data, augmentation, and regularization in vision transformers. In *TMLR*, 2022. 21, 22
- [75] Christian Szegedy, Wojciech Zaremba, Ilya Sutskever, Joan Bruna, Dumitru Erhan, Ian Goodfellow, and Rob Fergus. Intriguing properties of neural networks. In *ICLR*, 2014. 1, 2
- [76] Arash Vahdat, Karsten Kreis, and Jan Kautz. Score-based generative modeling in latent space. *NeurIPS*, 2021. 2, 12
- [77] Ashish Vaswani, Noam Shazeer, Niki Parmar, Jakob Uszkoreit, Llion Jones, Aidan N Gomez, Lukasz Kaiser, and Illia Polosukhin. Attention is all you need. In *NeurIPS*, 2017. 14
- [78] Joshua Vendrow, Saachi Jain, Logan Engstrom, and Aleksander Madry. Dataset interfaces: Diagnosing model failures using controllable counterfactual generation. *arXiv:2302.07865*, 2023. 1, 3
- [79] Sahil Verma, John P. Dickerson, and Keegan Hines. Counterfactual explanations for machine learning: A review. *arXiv preprint, arXiv:2010.10596*, 2020. 2
- [80] Sandra Wachter, Brent Mittelstadt, and Chris Russell. Counterfactual explanations without opening the black box: Automated decisions and the GDPR. *Harvard Journal of Law & Technology*, 2018. 2
- [81] C. Wah, S. Branson, P. Welinder, P. Perona, and S. Belongie. The caltech-ucsd birds-200-2011 dataset. Technical report, California Institute of Technology, 2011. 7, 22
- [82] Bram Wallace, Akash Gokul, Stefano Ermon, and Nikhil Naik. End-to-end diffusion latent optimization improves classifier guidance. *arXiv preprint arXiv:2303.13703*, 2023. 15
- [83] Lvmin Zhang and Maneesh Agrawala. Adding conditional control to text-to-image diffusion models. *arXiv preprint arXiv:2302.05543*, 2023. 3
- [84] Tianyuan Zhang and Zhanxing Zhu. Interpreting adversarially trained convolutional neural networks. *ICML*, 2019. 4

Appendix Summary

We start with a brief overview of the content of the Appendix.

In Appendix A, we give a more detailed description of diffusion models in general, cross-attention conditioning, classifier-free guidance, and our diffusion guidance via optimization.

The process of collecting real images to validate the detected zero-shot CLIP errors (see Fig. 5) is explained in Appendix B.

Appendix C is an extension of Section 6 from the main paper. We give further details about our visual counterfactual generation. Additionally, we show more VCEs for ImageNet (Fig. 16), CUB (Fig. 17), Food-101 (Fig. 18), Cars (Fig. 19) and FFHQ (Fig. 20).

Next, in Appendix D, we provide further details on our experiments from Sec. 4. In particular, the shape bias of adversarially robust models (Fig. 21), errors of zero-shot CLIP (Fig. 22) and different biases of ViT and ConvNeXt architectures (Fig. 23).

Appendix E contains more examples for our neuron visualizations of spurious neurons found in [68] (Fig. 24).

In Appendix F, we provide details on the user study comparing DVCEs [5] and our UVCEs, including all images that were used in the study (see Fig. 25 and Fig. 26).

A. Background and Method Details

A.1. Diffusion Models

Diffusion models are a class of generative models that learn to sample from a data distribution $q(x)$. We thereby differentiate between the forward process which, given a real data point, adds noise at every timestep $t \in \{1, \dots, T\}$ until the noisy sample can no longer be distinguished from a normally distributed random variable, and the reverse process, which, given a latent from a normal distribution, removes noise at every timestep such that at the final time step, we generate a sample $x \sim q(x)$. In short, the forward process takes a real data point to the latent space and the reverse process generates a real datapoint from a latent vector. For this section, we follow the notation from [72].

In this work, we focus on discrete-time diffusion models where both the reverse and forward process correspond to Markov Chains of length T and refer readers to [73] for the time-continuous case. While the first wave of image diffusion models [35, 71] were generating samples directly in pixel space, it has been shown [57, 76] that it can be beneficial to instead work inside the latent space of a variational autoencoder (VAE). Instead of generating the image directly, latent diffusion models (LDM) generate a latent z_0 inside the VAE latent space and then use the VAE decoder \mathcal{D} to transform z_0 into pixel space to produce the final image $x = \mathcal{D}(z_0)$. As our experiments are based on Stable Diffusion (SD) [57], for the rest of this section, we assume that

we are working with a latent diffusion model where the goal is to sample a VAE latent z_0 using the diffusion process.

Thus let $q(z_0)$ be the distribution of the VAE latents that can be obtained from the image distribution in pixel space $q(x)$ via the VAE encoder \mathcal{E} . The goal is to learn a model distribution $p_\theta(z_0)$ that is similar to the data distribution, i.e. $p_\theta(z_0) \approx q(z_0)$, and is easy to sample from. Denoising Diffusion Probabilistic Models (DDPM) [35] are defined via the forward process that uses Gaussian transitions $q(z_t|z_{t-1})$ to incrementally add noise to a noise-free starting latent z_0 :

$$q(z_t|z_{t-1}) = \mathcal{N}\left(z_t; \frac{\sqrt{\alpha_t}}{\sqrt{\alpha_{t-1}}}z_{t-1}, \left(1 - \frac{\alpha_t}{\alpha_{t-1}}\right)\mathbf{I}\right) \quad (7)$$

with a fixed decreasing sequence $\alpha_{1:T} \in (0, 1]^T$ that determines the noise-level at each time step t . Given z_0 , this defines a distribution over the other time steps $z_{1:T}$ via:

$$q(z_{1:T}|z_0) = \prod_{t=1}^T q(z_t|z_{t-1}). \quad (8)$$

Due to the Gaussian nature of the transitions $q(z_t|z_{t-1})$, given z_0 , it is possible to sample from $q(z_t|z_0)$ in closed-form instead of following the Markov chain t times via:

$$q(z_t|z_0) = \mathcal{N}\left(z_t, \sqrt{\alpha_t}z_0, (1 - \alpha_t)\mathbf{I}\right), \quad (9)$$

from which it follows that:

$$z_t = \sqrt{\alpha_t}z_0 + \sqrt{(1 - \alpha_t)}\epsilon, \quad \text{where } \epsilon \sim \mathcal{N}(0, \mathbf{I}). \quad (10)$$

This makes it obvious that, as long as α_T is chosen sufficiently close to 0, we have that $q(z_T|z_0) \approx \mathcal{N}(0, \mathbf{I})$, i.e. the forward process transforms the original distribution $q(z_0)$ into a standard Normal distribution. Thus one defines $p_\theta(z_T) = \mathcal{N}(0, \mathbf{I})$ as the prior distribution for the generative model. Our parameterized distribution over the noise-free latents $p_\theta(z_0)$ is then defined as:

$$p_\theta(z_0) = \int p_\theta(z_{0:T}) dz_{1:T} \quad (11)$$

with $p_\theta(z_{0:T}) = p_\theta(z_T) \prod_{t=1}^T p_\theta^{(t)}(z_{t-1}|z_t).$

The goal in training a diffusion model is thus to optimize the parameters θ that are used to parameterize the *reverse* transitions $p_\theta^{(t)}(z_{t-1}|z_t)$, which intuitively remove some of the noise from z_t , such that $p_\theta(z_0) \approx q(z_0)$. One key finding from [71] is that in the limit of $T \rightarrow \infty$, the reverse transitions become Gaussians with diagonal covariance matrix, thus in practice all *reverse* transitions $p_\theta^{(t)}(z_{t-1}|z_t)$ are assumed to be diagonal Gaussian distributions where the mean

and covariance are parameterized using a DNN. Originally, diffusion models were trained by optimizing the parameters of the model that is used to predict the means and covariance matrices of those reverse transitions to maximize the variational lower bound [71].

[35] found that, if one uses fixed covariances for the *reverse* transitions, it is possible to instead optimize a loss function that resembles a weighted denoising objective:

$$L(\theta) = \sum_{t=1}^T \gamma_t \mathbb{E}_{z_0 \sim q(z_0), \epsilon \sim N(0, \mathbf{I})} \left[\|\epsilon_{\theta}^{(t)}(\sqrt{\alpha_t} z_0 + \sqrt{1 - \alpha_t} \epsilon) - \epsilon\|_2^2 \right]. \quad (12)$$

Here, $\epsilon_{\theta}^{(t)}$ is a denoising model that, given a noisy latent $\sqrt{\alpha_t} z_0 + \sqrt{1 - \alpha_t} \epsilon$ at time step t , tries to predict the added noise ϵ , and $(\gamma_t)_{t=1}^T$ is a sequence of weights for the individual time steps that depend on $(\alpha_t)_{t=1}^T$. In practice, all $\epsilon_{\theta}^{(t)}$ are parameterized using a single U-Net which is given the current time step t as additional input, i.e. $\epsilon_{\theta}^{(t)}(z) := \epsilon_{\theta}(z, t)$.

Once ϵ_{θ} has been trained, there are multiple samplers that allow us to obtain a new latent z_0 . In all cases, one starts by sampling from the prior distribution $z_T \sim \mathcal{N}(0, \mathbf{I})$. For this work, we focus on the DDIM solver, which is a deterministic solver, i.e. all the randomness of the process lies in z_T whereas the rest of the chain $z_{0:(T-1)}$ are fully determined by z_T . The update rule for DDIM is:

$$z_{t-1} = \frac{\sqrt{\alpha_{t-1}} z_t - \sqrt{1 - \alpha_t} \epsilon_{\theta}(z_t, t)}{\sqrt{\alpha_t}} + \sqrt{1 - \alpha_{t-1}} \epsilon_{\theta}(z_t, t). \quad (13)$$

DDIM can best be understood from Eq. (10) by assuming that $\epsilon = \epsilon_{\theta}(z_t, t)$ and solving for z_0 . Intuitively, this is equivalent to skipping all intermediate time steps and jumping directly from z_t to z_0 :

$$z_0 = \frac{z_t - \sqrt{(1 - \alpha_t) \epsilon_{\theta}(z_t, t)}}{\sqrt{\alpha_t}}. \quad (14)$$

Now if we apply Eq. (10) to our estimate of z_0 to get to time step $t - 1$ and again use our noise estimate $\epsilon = \epsilon_{\theta}(z_t, t)$, we can recover the DDIM update rule. More formally, DDIM sampling is related to solving the probability flow ODE introduced in [73] using the Euler method, see Proposition 1 in [72]. Considering the connection between ODEs and ResNets described in [16], it is not surprising that the DDIM updates have the residual connection that allows for easy

gradient flow through diffusion graphs:

$$z_{t-1} = \frac{\sqrt{\alpha_{t-1}}}{\sqrt{\alpha_t}} z_t + F(z_t, t),$$

$$\text{where } F(z_t, t) = \left(1 - \frac{\sqrt{\alpha_{t-1}}}{\sqrt{\alpha_t}}\right) \sqrt{1 - \alpha_{t-1}} \epsilon_{\theta}(z_t, t). \quad (15)$$

A.2. Conditional Diffusion Models

While the previous Section introduced unconditional latent diffusion models, i.e. models that learn a distribution $p_{\theta}(z)$, in practice it is often desirable to work with conditional models that give the user control over the output of the diffusion model. For example, if we are using an image dataset like ImageNet, the conditioning could be the target class we want to generate, or for the popular text-to-image models like Stable Diffusion [57], the conditioning will be a text prompt that tells the diffusion model what image it should generate.

A.3. Classifier-Free Guidance and Cross-Attention Conditioning

Classifier-free guidance (CFG) [33] was introduced as an alternative to classifier guidance [9, 40, 49, 73]. [18] already used a class-conditional denoising model $\epsilon_{\theta}(x_t, t, y)$ that was given the target class as additional input. The class label y was thereby integrated into the model via adaptive group normalization layers. They introduced classifier guidance to enforce the generation of the correct target class by strengthening the influence of y on the output of the generative process. Classifier-free guidance is an alternative that also strengthens the impact of the conditioning signal in combination with a conditional denoising model $\epsilon_{\theta}(x_t, t, y)$ without the requirement of an external classifier.

In the following, we will first introduce cross-attention (XA) conditioning that is used by Stable Diffusion [57] to condition the denoising model ϵ_{θ} not only on class labels but also other modalities such as text prompts or depth maps. Then we will introduce classifier-free Guidance as a solution to strengthen the impact of the conditioning signal.

A.3.1 Cross-Attention Conditioning

As our work is based on text-to-image Stable Diffusion [57], we restrict ourselves to text conditioning in the following Section. Thus assume that we are given a text prompt P , for example, "an image of a dog on the beach". The first step in creating a text-to-image diffusion model is to encode the prompt using a domain-specific encoder τ . In the case of Stable Diffusion 1.4, τ is a pre-trained CLIP [52] ViT-L/14 [19] text encoder as suggested in the Imagen paper [60]. Using τ , one can transform the prompt P into a conditioning matrix $C \in \mathbb{R}^{N_c \times d_{\tau}}$, where N_c corresponds to the number

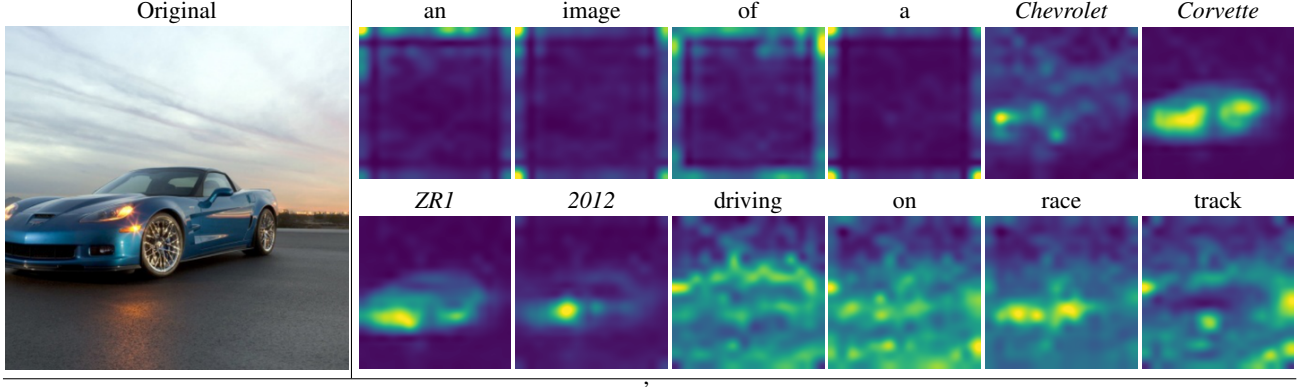


Figure 13. Visualization of the cross-attention maps produced from an image from the Cars validation set that was captioned by OpenFlamingo as "an image of a Chevrolet Corvette ZR1 2012 driving on a race track" and inverted via Null-Text inversion [46]. Given the starting latent z_T and the null-text sequence, $(\emptyset_t)_{t=1}^T$ from the inversion, we reconstruct the image using 50 DDIM steps and save the XA maps M from the cross-attention layers inside the denoising U-Net. We show the cross-attention maps corresponding to each word for the first half of the diffusion process ($T : (T/2)$) obtained at spatial resolution 16×16 inside the U-Net averaged across all attention heads, normalized to $[0, 1]$ and upsampled to 512×512 . Note that the XA maps corresponding to the class name "Chevrolet Corvette ZR1 2012" can be used to locate the car in the image.

of tokens that the prompt P is split into and d_τ is the output feature dimension of the CLIP encoder.

In SD, the conditioning C is fed into to the denoising U-Net [58] model $\epsilon_\theta(z_t, t, C)$ via cross-attention (XA) layers [77]. In those XA layers, the visual features of the internal representations of the current latent z_t inside the U-Net are fused with the encoded text conditioning C to generate a noise estimate $\epsilon_\theta(z_t, t, C)$ that will not only lead us to the image manifold but also incorporate the text features. In detail, let $\phi_i(z_t)$ denote the intermediate representations inside the U-Net of the latent z_t at time step t that are fed into the i -th XA layer. As usual in attention layers, $\phi_i(z_t)$ is decoded into a query matrix $Q^{(i)}$ via a linear transformation with weight matrix $W_Q^{(i)}$. Similarly, the conditioning C is projected into key and value matrices $K^{(i)}$ and $V^{(i)}$ using the weight matrices $W_K^{(i)}$ and $W_V^{(i)}$. The XA operation for query, key and value matrices Q, K, V is then defined as:

$$\begin{aligned} \text{XA}(Q, K, V) &= M \cdot V, \\ \text{where } M &= \text{softmax}\left(\frac{QK^T}{\sqrt{d}}\right). \end{aligned} \quad (16)$$

During training, the SD model is trained on a dataset containing image-text pairs and the conditioning vector C obtained from the text prompt is given to the denoising model. This leads ϵ_θ to learn to use the information in C to generate a noise estimate that points to images corresponding to the conditioning information instead of the general image manifold. In practice, each attention Layer in the U-Net is implemented as multi-head attention where the attention is done multiple times in parallel and then combined to the

final output via an additional linear transformation. Intuitively, as Q is a representation of the visual features from z_t and K is a representation of the textual features from the original prompt P , the output of the softmax function M can be interpreted as a similarity between visual features and text features. In particular, large entries in M correspond to spatial locations that are heavily influenced by a particular text token. We show a visual example for this in Figure 13, where we plot the XA maps obtained from reconstructing an inverted image from the Cars validation set that we use for visual counterfactual generation in Figure 9. We use the strong spatial localization in the XA maps to generate a foreground segmentation mask for our distance regularization when creating VCEs (See Section 6 and C).

A.3.2 Classifier-Free Guidance

Even with the conditional denoising model $\epsilon_\theta(z_t, t, C)$, it can happen that the generated images do not follow the conditioning C close enough. Classifier-free guidance was therefore introduced to strengthen the impact of C . To do so, the denoising model is jointly trained on images *without* text prompt and the conditioning C for all of those images is replaced by the CLIP encoding of the empty string to create the null-token $\emptyset := \tau("")$. Intuitively $\epsilon_\theta(z_t, t, C)$ then points to the direction of noise-free images that correspond to the prompt C whereas $\epsilon_\theta(z_t, t, \emptyset)$ is an unconditional noise-estimate. The estimated noise ϵ in Eq. (1) is then replaced with the classifier-free version $\hat{\epsilon}$

$$\begin{aligned} \hat{\epsilon}(z_t, t, C, \emptyset) &= \epsilon_\theta(z_t, t, C) \\ &\quad + w (\epsilon_\theta(z_t, t, C) - \epsilon_\theta(z_t, t, \emptyset)), \end{aligned} \quad (17)$$

where w in Eq. (17) corresponds to the classifier-free guidance strength.

A.4. Diffusion Guidance via Optimization

Next, we present some additional details about our diffusion optimization. Remember from Sec. 3.2 that our goal is to find inputs to the diffusion process $z_T, (C_t)_{t=1}^T, (\emptyset_t)_{t=1}^T$ which optimize an objective like Eq. (2).

As usual, we want to use a first-order optimizer like ADAM which requires us to calculate the gradients of the loss with respect to the input variables. Since DDIM requires at least 20 steps to yield high-quality images, it is not possible to store the entire diffusion graph for backpropagation due to memory limitations. This problem can easily be circumvented by using gradient checkpointing which allows us to calculate the exact gradients of the objective with respect to the optimization variables.

In addition, some readers might recognize the similarity between our optimization formulation and that of adversarial attacks. In general, we found the diffusion model to be a strong prior for the creation of meaningful changes instead of adversarial perturbations. Note that this behavior is not unexpected as it has been demonstrated that diffusion models can be used for adversarial purification [50]. This means that the combination of a non-adversarially robust classifier and a denoising diffusion model yields a classification pipeline with non-trivial robustness to adversarial attacks and it has been demonstrated that robust models have certain generative properties [6]. To further prevent the generation of adversarial examples, we found it helpful to use test-time augmentations on our generated images before forwarding them through the classifier f for gradient computations. In particular, we found that generating different views of the same input image and averaging the loss over all of them yields more meaningful changes. In this work, we combine two types of augmentations. First, we randomly cutout different crops from the image [82] and then add Gaussian noise to each crop. In Fig. 14, we demonstrate that this yields gradients (with respect to the input image in pixel space) that are much more localized on the class object of interest.

B. Validation of zero-shot CLIP errors

To validate the errors found in Fig. 5, we collected similar real images from the LAION-5B dataset using the CLIP retrieval tool¹. The used retrieval queries were of the form “an image of ...” and resemble the detected failure cases: “... a waffle” for “waffle iron”, “... an arch bridge” for “steel arch bridge”, “... a spoon on a wooden table” for “wooden spoon” and “... a bar in space” for “space bar”. For “steel arch bridge” and “wooden spoon”, this procedure finds many images confirming the observed failure case. In the case of

¹<https://knn5.laion.ai>

“waffle iron”, some kinds of waffles also produce a high confidence for the ConvNeXt as this feature is probably also spuriously correlated in the ImageNet training data. The “space bar” example is very specific and the retrieval procedure returns only few images fitting the pattern.

C. Visual Counterfactual Explanations

C.1. Method Details

We start by giving a more detailed description of our universal visual counterfactual explanation (UVCE) method and motivate our design choices. As in the main paper, we assume we are given a starting image from the validation set \hat{x} belonging to class \hat{y} and our goal is to create a VCE x that is classified as target class y by the classifier f . In the next subsections, we go over the individual steps of the UVCE process. The UVCE generation can be split into the following parts:

- i) Create a caption of the image using OpenFlamingo
- ii) Invert the image using Null-Text inversion
- iii) Obtain XA maps and compute foreground mask
- iv) Optimize the confidence into the target class and background similarity to the original image

Additionally, we show a diagram linking the individual parts to each other in Fig. 15 and give an algorithmic overview in Algorithm 2.

C.1.1 Captioning

As every DDIM inversion requires a prompt, we first have to generate a prompt that describes \hat{x} . As we are going to use the XA maps to create a foreground segmentation map, it is important to have an accurate description of both the foreground object but also the background, such that in the XA layers, only the spatial locations in the image belonging to the class object attend to words from the class name corresponding to \hat{y} , which we call `<ORIGINAL CLASSNAME>`. We found that using the generic caption “an image of a `<ORIGINAL CLASSNAME>`” results in worse post-inversion reconstruction qualities and can result in words contained in the class name attending to locations in the background of the image as these background objects do not have matching descriptions in the generic caption. We, therefore, use Open-Flamingo [3, 7] to enhance the generic captions. In particular, we manually label less than 30 images from the training set and always use the form: “an image of a `<ORIGINAL CLASSNAME>` `<BACKGROUND DESCRIPTION>`”, for example, “an image of a koala hanging on a tree”. We can then use the Flamingo model to take the image \hat{x} with the generic prompt “an image of a `<ORIGINAL CLASSNAME>`” as input and add a background de-

Algorithm 1 Diffusion Guidance via Optimization

Input: Loss function L , Initial Prompt P , number of iterations K
 $z_T \sim \mathcal{N}(0, 1)$ ▷ Draw starting latent
 $C = \tau(P)$ ▷ Encode prompt
 $\emptyset = \tau(" ")$ ▷ Generic null-text

for $t = 1, \dots, T$ **do** ▷ Initialize time step-dependent variables
 $C_t = C$
 $\emptyset_t = \emptyset$
end for
 $\text{optim} = \text{Adam}(z_T, C_1, \dots, C_T, \emptyset_1, \dots, \emptyset_T)$ ▷ Define the optimizer

for $k = 1, \dots, K$ **do** ▷ Optimization loop
 $z = z_T$
for $t = T, \dots, 1$ **do** ▷ Denoising DDIM loop
with `gradient_checkpointing()`:
 $\hat{\epsilon} = \epsilon_\theta(z, t, C_t) + w (\epsilon_\theta(z, t, C_t) - \epsilon_\theta(z, t, \emptyset_t))$ ▷ CFG update (17)
 $z = \sqrt{\alpha_t} \frac{z - \sqrt{1-\alpha_t} \hat{\epsilon}}{\sqrt{\alpha_t}} + \sqrt{1 - \alpha_t} \hat{\epsilon}$ ▷ DDIM step (13)
end for

 $x = \mathcal{D}(z)$ ▷ Decode final latent using VAE decoder
 $l = L(x)$ ▷ Calculate loss l
 $l.\text{backward}()$ ▷ Calculate gradients

 $\text{optim.step}()$
 $\text{optim.zero_grad}()$
end for
return $z_T, (C_t)_{t=1}^T, (\emptyset_t)_{t=1}^T$

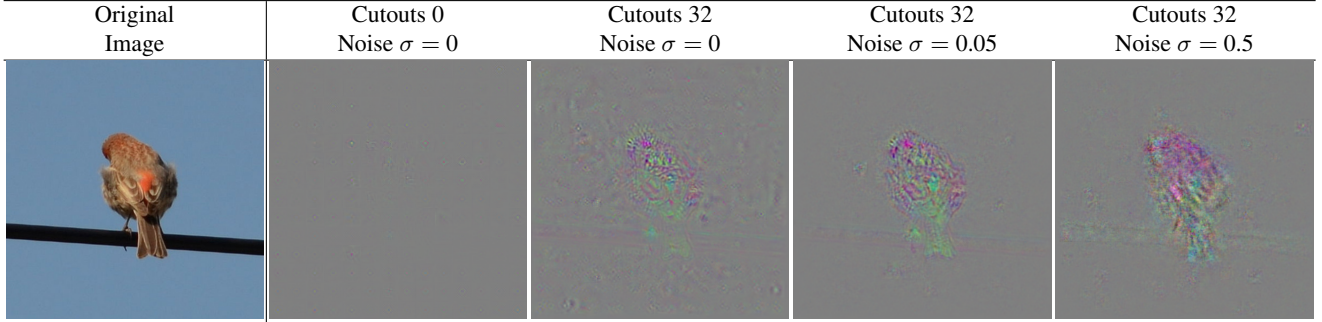


Figure 14. We plot the gradient $\nabla_x p_f(y|x)$ with different test-time augmentations, including Cutout and Gaussian Noise with two standard deviations. The classifier f is a ViT and the original image is an ImageNet validation image for the class "house finch" and the target class y is "gold finch". Note that the gradient without augmentation is very noisy and not located on the bird. If we average the gradient across slightly perturbed images, we can achieve localization on the foreground object. While adding noise on top of the Cutout augmentation can further improve localization, too much noise ($\sigma = 0.5$) leads to very coarse gradients that are no longer usable for optimization. Each gradient is separately rescaled to fit in $[0, 1]$ and grey values of 0.5 correspond to a zero gradient.

scription that resembles our handcrafted ones. We call the resulting prompt \hat{P} . In particular, due to its construction, \hat{P} is guaranteed to contain the name of the starting class.

To use \hat{P} as conditioning within the Stable Diffusion pipeline, we then encode the prompt \hat{P} into its representation

$$\hat{C} = \tau(\hat{P}) \text{ using the CLIP text encoder } \tau.$$

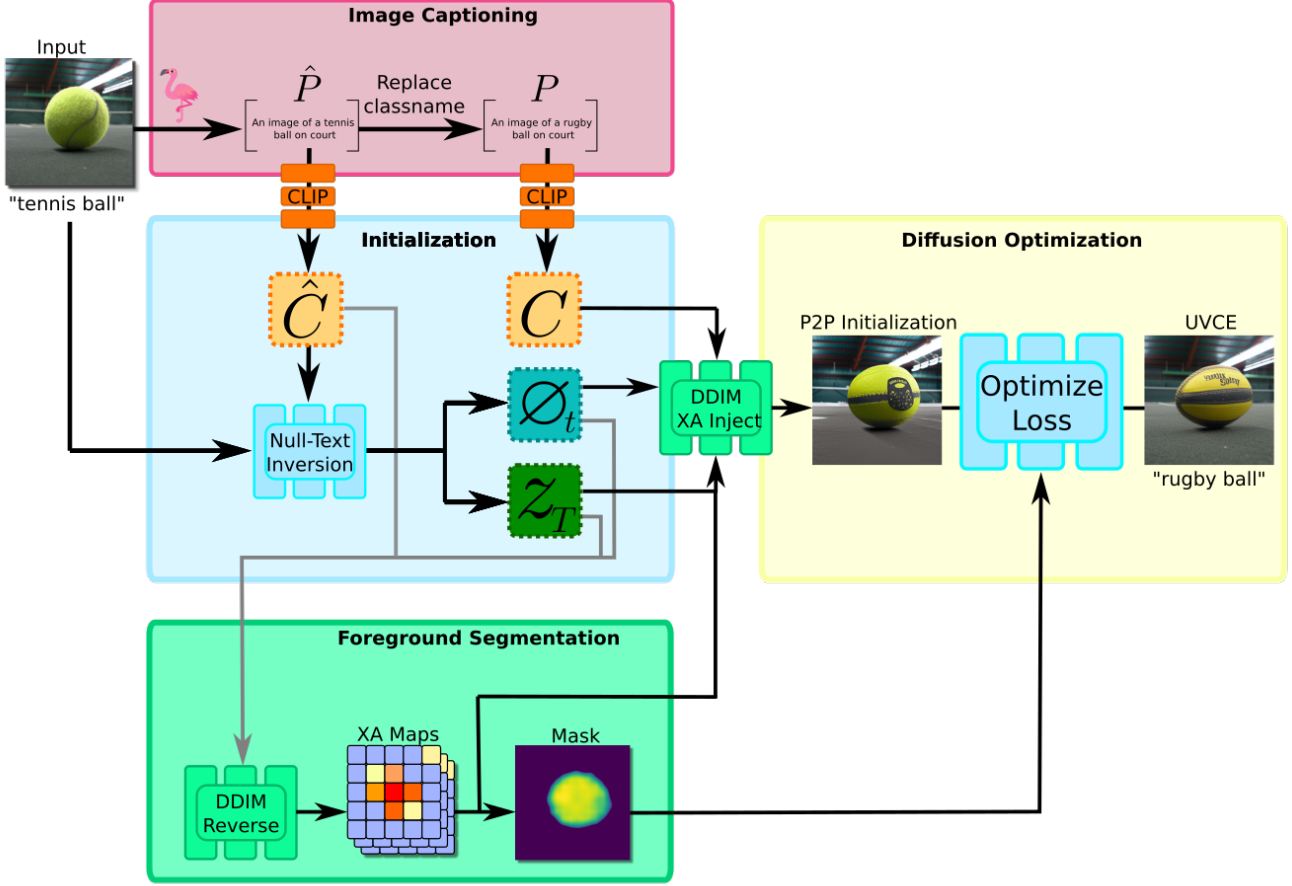


Figure 15. A graphical representation of our UVCE generation. We start with the input image and caption it using OpenFlamingo to get a prompt \hat{P} . A new prompt P containing the target class name is generated via string replacement. Both are encoded via the CLIP text model to get the conditionings \hat{C} and C belonging to the original and target class names. We then use Null-Text inversion with the *original* prompt \hat{C} to get a starting latent z_T and null-text sequence $(\phi_t)_{t=1}^T$ which can be used to re-generate the input image. We then run the standard DDIM denoising process using z_T , \hat{C} and $(\phi_t)_{t=1}^T$ which will restore the original image and allows us to capture the Cross-Attention (XA) maps. These can be used to produce a foreground segmentation mask. The initialization for our optimization is obtained by replacing the original conditioning \hat{C} with the new conditioning C and by using prompt-to-prompt-like XA injection using the stored XA maps. As the resulting image will often have low confidence in the target class and/or be too far away from the input image, we optimize z_T , $(C_t)_{t=1}^T$ and $(\phi_t)_{t=1}^T$ using the ADAM optimizer to obtain our final UVCE.

C.1.2 Inversion:

Next, we have to invert \hat{x} , i.e. find a latent z_T that, together with the conditioning \hat{C} reconstructs the original image. The standard DDIM inversion [72] often results in bad inversions that do not recreate \hat{x} . We, therefore, use Null-Text inversion [46], which uses the DDIM inversion with its latent z_T as initialization and then optimizes the null-text tokens $(\phi_t)_{t=1}^T$ such that the image resulting from the diffusion process matches the original image \hat{x} , i.e. $\hat{x} \approx \mathcal{D}(\mathbf{z}_0(z_T, \hat{C}, (\phi_t)_{t=1}^T))$, where we use \mathbf{z}_0 for the function that takes a starting latent z_T , conditioning matrix \hat{C} and the null-text sequence $(\phi_t)_{t=1}^T$ and returns the final latent obtained from running the entire diffusion process.

C.1.3 Initialization using XA-injections

Our objective is to create an image x that is similar to \hat{x} but shows an object from the new target class y . To achieve this, we can make use of the knowledge contained in SD to find a better initialization in the CLIP encoding space. A good initialization is important because our optimization problem is highly non-convex, thus the initialization will directly influence the resulting image as we can not guarantee convergence to the global minimum and also, we are interested in producing images with as few optimization steps as possible. It is thus natural to take the original prompt \hat{P} and create a new prompt P by replacing the name of the starting class <ORIGINAL CLASSNAME> with the name of the tar-

Algorithm 2 VCE Generation

Input: Input image \hat{x} , Starting class \hat{y} , Target class y , number of iterations K , Classifier f

start_classname = ClassNames[\hat{y}] ▷ Create prompts
target_classname = ClassNames[y]
 \hat{P} = open_flamingo(\hat{x} , "an image of a" + start_classname)
 P = \hat{P} .replace(start_classname, target_classname)

$\hat{C} = \tau(\hat{P})$ ▷ CLIP Encode prompts
 $C = \tau(P)$

$z_{\text{Original}}, \emptyset_1, \dots, \emptyset_T = \text{null_text_inversion}(\hat{x}, \hat{C})$ ▷ Invert Image
 $z_T = z_{\text{Original}}.\text{clone}().\text{detach}()$

$\text{xa_maps} = \text{ddim_loop_extract_xa}(z_T, \hat{C}, \emptyset_1, \dots, \emptyset_T)$ ▷ Extract Cross-Attention maps
 $S_{\text{PX}}, S_{\text{VAE}} = \text{make_segmentation_from_xa}(\text{xa_maps})$ ▷ Get Pixel and latent space masks

for $t = 1, \dots, T$ **do** ▷ Initialize time step-dependent conditioning
 $C_t = C$
end for

$\text{optim} = \text{Adam}(z_T, C_1, \dots, C_T, \emptyset_1, \dots, \emptyset_T)$ ▷ Define the optimizer

for $k = 1, \dots, K$ **do** ▷ Optimization loop
 $z = z_T$
 $z_0 = \text{ddim_loop_xa_inject}(z_T, C_1, \dots, C_T, \emptyset_1, \dots, \emptyset_T, \text{xa_maps})$

$x = \mathcal{D}(z_0)$ ▷ Decode final latent using VAE decoder
 $l_{\text{CE}} = -\log p_f(y|x)$ ▷ Calculate losses
 $l_d = w_{\text{VAE}} \|(1 - S_{\text{VAE}}) \odot (z_0 - z_{\text{Original}})\|_2^2 + w_{\text{PX}} \|(1 - S_{\text{PX}}) \odot (x - \hat{x})\|_2^2$
 $l = l_{\text{CE}} + l_d$
 $l.\text{backward}()$ ▷ Calculate gradients

$\text{optim.step}()$
 $\text{optim.zero_grad}()$

end for
return $z_T, (C_t)_{t=1}^T, (\emptyset_t)_{t=1}^T$

get class <TARGET CLASSNAME>. After encoding using the CLIP encoder τ , we then get an additional conditioning $C = \tau(P)$, corresponding to the prompt containing the label of the target class y .

Note that the Null-Text inversion naturally results in a time-step-dependent sequence of null-text tokens $(\emptyset_t)_{t=1}^T$, which is why we also adopted time-step-dependent conditioning $(C_t)_{t=1}^T$ to have the same degrees of freedom in both the null-text and the conditioning during optimization. We initialize $C_t = C$ for all t .

The issue is that even local changes in the conditioning tend to have a global impact on the final image, which will lead to $\mathcal{D}(z_0(z_T, C, (\emptyset_t)_{t=1}^T))$ looking very different from $\mathcal{D}(z_0(z_T, \hat{C}, (\emptyset_t)_{t=1}^T))$, not only in the foreground but also in the background (we refer readers to Figure 5 in the orig-

inal Prompt-to-Prompt paper [31] for a visualization). As our goal is to create a VCE that resembles the original image, this is highly undesirable as we would have to spend many optimization steps to minimize the distance in the background between our new image and the starting image.

[31] found that the overall image structure is mostly dictated by the first diffusion steps and the XA maps inside the denoising U-Net ϵ . It is thus possible to preserve the overall image structure by injecting the XA maps that lead to the creation of one image when creating a new image with a modified prompt. Recall from Section A.3.1 that inside the i -th XA layer in the U-Net, we compute a weight matrix $M^{(i)}$ that measures similarity between the U-Net encoded spatial features from the current latent $\phi_i(z_t)$ and the encoded text prompt C_t . In detail, $M^{(i)}$ corresponds to the softmax-normalized similarity between:

- The query matrix $Q^{(i)}$, i.e. the projected internal representation of z_t inside the U-Net $W_Q^{(i)} \cdot \phi_i(z_t)$ where the number of rows corresponds to the spatial resolution of the output of ϕ_i , e.g. $16 \times 16 = 256$. We call this spatial resolution N_{ϕ_i} .
- The key matrix $K^{(i)}$, i.e. the projected conditioning C_t at time step t : $W_K^{(i)} \cdot C_t$. The number of rows in $K^{(i)}$ corresponds to the number of tokens N_c that the prompt was split into in the tokenizer of the CLIP encoder.

As $M^{(i)}$ is defined as the post softmax output of $Q^{(i)} \cdot (K^{(i)})^T$, $M^{(i)}$ is a matrix of size $N_{\phi_i} \times N_c$. The (j, k) -th entry can therefore be interpreted as the similarity between the spatial features at position j in the flattened version of $\phi_i(z_t)$ and the k -th token in the conditioning matrix C_t . Now let $\hat{M}_t^{(i)}$ correspond to the XA maps that can be obtained from the i -th XA layer inside the denoising U-Net at time step t when running the diffusion process with the *original* conditioning \hat{C} . Due to the null-text inversion, this diffusion process will nearly perfectly reconstruct the original image \hat{x} and thus the XA maps $\hat{M}_t^{(i)}$ will capture the structure of the *original* image.

During optimization, we now want to re-inject those XA maps when using our modified conditioning sequence $(C_t)_{t=1}^T$. Let $M_t^{(i)}$ denote the *new* XA maps at time step t at the i -th XA layer of the U-Net that corresponds to the similarity between the spatial features and tokens belonging to the current conditioning C_t being optimized instead of the original conditioning \hat{C} . [31] found that it is not necessary to inject the original XA maps \hat{M} throughout the entire diffusion process and therefore only did the XA injection for a certain part of the diffusion process. In our case, we replace the XA maps for the first 80% of denoising steps.

Note that the original Prompt-to-Prompt implementation only supports the replacement of words in a 1-to-1 fashion. However, in our case, <ORIGINAL CLASSNAME> and <TARGET CLASSNAME> can have a different number of words. We, therefore, calculate a similarity matrix that measures the cosine distance between all words in both strings in CLIP embedding space (if a word is encoded into multiple tokens, we average all of them to get a word-level representation in the CLIP latent space) and use these distances to reshape $\hat{M}_t^{(i)}$ into a matrix that has the same size as $M_t^{(i)}$ via weighted averaging.

C.1.4 Distance regularization and Optimization

Given z_T , $(C_t)_{t=1}^T$ and $(\emptyset_t)_{t=1}^T$ and the original XA maps $\hat{M}_t^{(i)}$ we can finally define our optimization objective as in Eq. (6). Our new initialization will show class features from y and be relatively similar to \hat{x} , however, as we show in Figure 11, the resulting images often have quite low confidence in the target class y and non-localized changes. Optimizing

the confidence can again be done by maximizing $\log p_f(y|x)$. For the distance regularization, we use the segmentation-based regularization described in the main paper in Eq. (5).

As noted previously, we can use the XA maps to get an idea of the location of the object in the image. Typically, the overall structure is captured best by the XA maps corresponding to the earlier diffusion steps. We, therefore, average the initial XA maps $\hat{M}_t^{(i)}$ from the first half of the diffusion process at resolution 16×16 in the U-Net that belong to all tokens that correspond to the words in <ORIGINAL CLASSNAME> to approximate the location of the object in the image (see also Figure 13). For example, for the dog breed "Cocker Spaniel", we average the XA maps that correspond to the 3 tokens that the CLIP tokenizer uses to encode this class name. We then normalize these to have a maximum value of 1 to get our foreground segmentation which can then be upsampled to the spatial sizes of the VAE latent to obtain the mask S_{VAE} as well as pixel space size to get the mask S_{PX} . Given those masks, we can define our regularizer as:

$$d(z, \hat{x}) = w_{\text{VAE}} \|(1 - S_{\text{VAE}}) \odot (z - \mathcal{E}(\hat{x}))\|_2^2 + w_{\text{PX}} \|(1 - S_{\text{PX}}) \odot (\mathcal{D}(z) - \hat{x})\|_2^2. \quad (18)$$

With this masked distance regularizer, we allow our optimization to arbitrarily change the foreground object, for example, it allows us to have large color changes that are not achievable with standard l_p regularization while still enforcing a strong similarity in the background of the image. We emphasize that it is important to have an accurate description of the background to make sure that background pixels are not captured by words in the class name, which is why it is important to use detailed Flamingo captions instead of generic ones.

Given the foreground mask, we optimize the starting latent z_T , our modified prompt embedding $(C_t)_{t=1}^T$, and the null-text sequence $(\emptyset_t)_{t=1}^T$ to maximize the objective given in Eq. (6).

C.1.5 Hyperparameters

The hyperparameters are *identical* across all UVCE tasks and images presented in this paper. This shows that our method can adapt to a large variety of image configurations and supports new classifiers as well as very different image datasets without any hyperparameter tuning.

Resolution	512
Guidance Scale	3.0
DDIM steps	20
Optimizer	ADAM
Optimization steps	20
C_t, \varnothing_t stepsize	0.01
z_T stepsize	0.001
Scheduler	\times
Gradient Clipping	\times
w_{VAE}	25.0
w_{PX}	250.0
Num. cutouts	16
Cutout Noise σ	0.005

C.2. Qualitative Result

In Figure 16 we show additional qualitative results on ImageNet where we compare our UVCEs to DVCEs [5] in the generation of classes that are close in the WordNet hierarchy. As the classifier, we use the same ViT-B as in the main paper. We again demonstrate that we are able to generate highly realistic looking UVCEs with minimal background changes that achieve high confidence in the target class. Unlike DVCEs, we cannot only handle texture changes but also more complex class changes that require editing the geometry of the image. For a selection of *random* images, please also refer to Fig. 25 and Fig. 26 which show the randomly selected images for the user study.

Additionally, in Fig. 17, Fig. 18 and Fig. 19, we present additional VCEs in a more fine-grained context for the CUB, Food-101 and Cars datasets. The classifiers are the same as in Fig. 10, namely a CAL-ResNet101 [55] classifier for Cars, a fine-tuned ViTMAE [27] for CUB and a fine-tuned ViT on Food-101. Our broad model selection shows that our UVCEs cannot only be used to explain standard vision transformers but also support models with different pre-training strategies as well as convolutional neural networks without adjusting hyperparameters. Note that DVCEs only support ImageNet due to the requirement for a diffusion model trained on that dataset and a robust classifier trained on the specific dataset which are not available for the CUB, Cars, or Food-101 datasets. Similar to ImageNet, we are able to create highly realistic VCEs that can handle very fine-grained class changes which cannot be achieved via textural changes that also preserve the image background due to our background distance regularization.

C.2.1 Zero-Shot Attribute VCEs

Lastly, we demonstrate UVCEs for zero-shot attribution classification using a CLIP model.

Assume we want to create a counterfactual that changes a certain source attribute to a target attribute in an image, for example, "smiling" to "looking sad" for a zero-shot attribute

classifier. We first describe how we turn the CLIP model into a binary zero-shot classifier for this particular image \hat{x} and attribute. We again start with a prompt \hat{P} that contains the textual description of the source attribute and image, for example, "a closeup portrait of a man smiling". We then replace the source with the target attribute to obtain P , in this case, "a closeup portrait of a man looking sad". Note that we use the same prompts \hat{P} and P for the zero-shot classification as well as the DDIM inversion and UVCE generation.

Next, both prompts are encoded by the *text* encoder of the CLIP model f_{txt} . Given an input image x , we decode it using the *image* encoder f_{im} . Now we can calculate the logits for the two classes (corresponding to the target and source attribute) as:

$$\langle f_{\text{txt}}(P), f_{\text{im}}(x) \rangle \quad \text{and} \quad \langle f_{\text{txt}}(\hat{P}), f_{\text{im}}(x) \rangle \quad (19)$$

The log-probability of the binary zero-shot classifier detecting the target attribute is thus given by:

$$\log \frac{\exp(\langle f_{\text{txt}}(P), f_{\text{im}}(x) \rangle)}{\exp(\langle f_{\text{txt}}(P), f_{\text{im}}(x) \rangle) + \exp(\langle f_{\text{txt}}(\hat{P}), f_{\text{im}}(x) \rangle)}. \quad (20)$$

For the examples in Fig. 20, we use face images from FFHQ [37] and the OpenCLIP [34] implementation of the CLIPA [41] ViT-H/14 trained on DataComp-1B [22]. Faces are generally challenging for VCEs as humans are naturally good at recognizing minor modifications between the generated and original image. Still, our examples demonstrate that we can create highly realistic UVCEs that only change the source to the target attribute while preserving the overall facial structure. In particular, for all examples, the person in the generated image can clearly be identified to be the same as the one in the starting image and the faces look realistic without any artifacts.

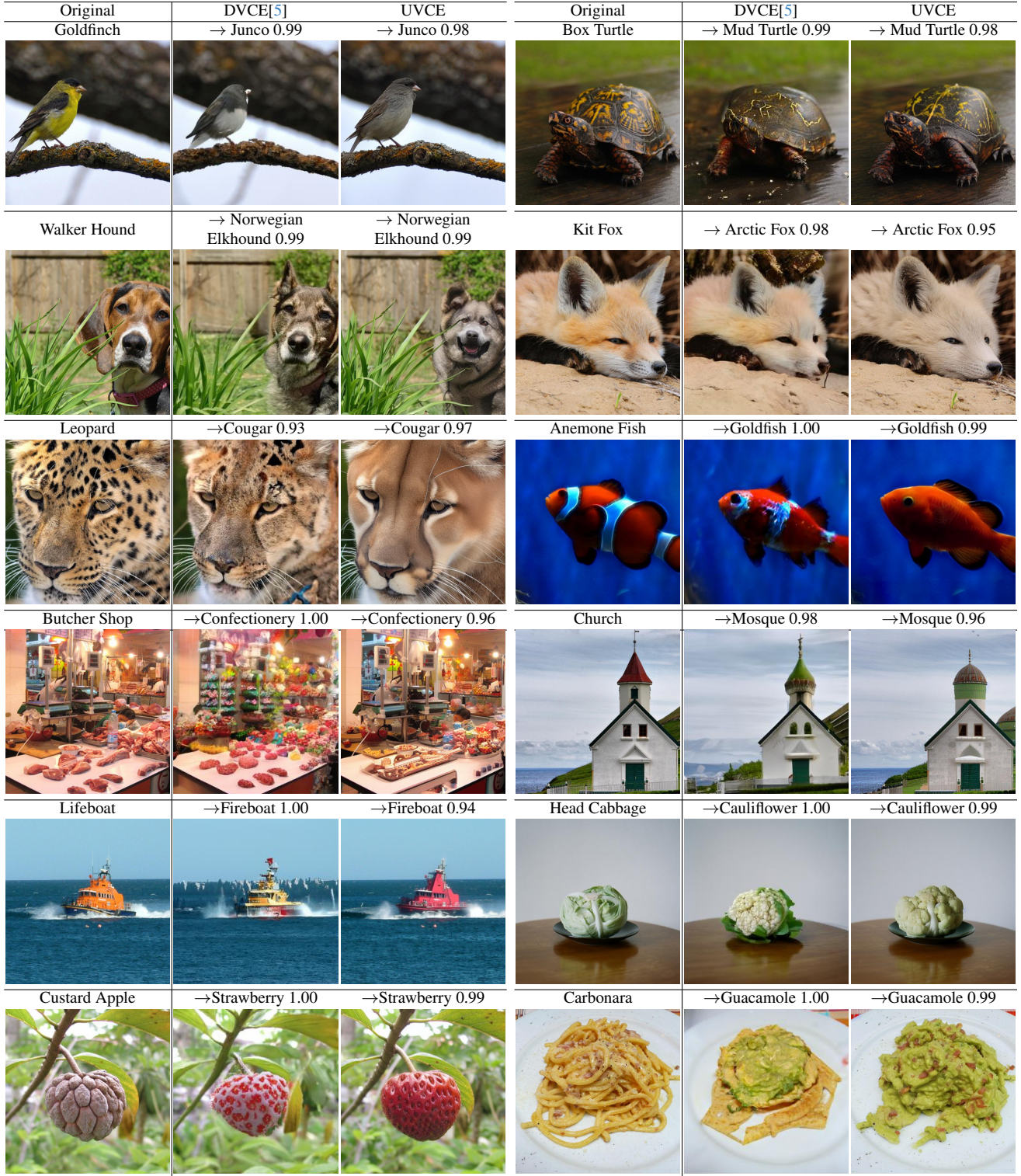


Figure 16. **ImageNet-1K** [59] UVCEs for a ViT-B/16 AugReg [19, 74] pretrained on ImageNet-21K and fine-tuned on ImageNet-1K.

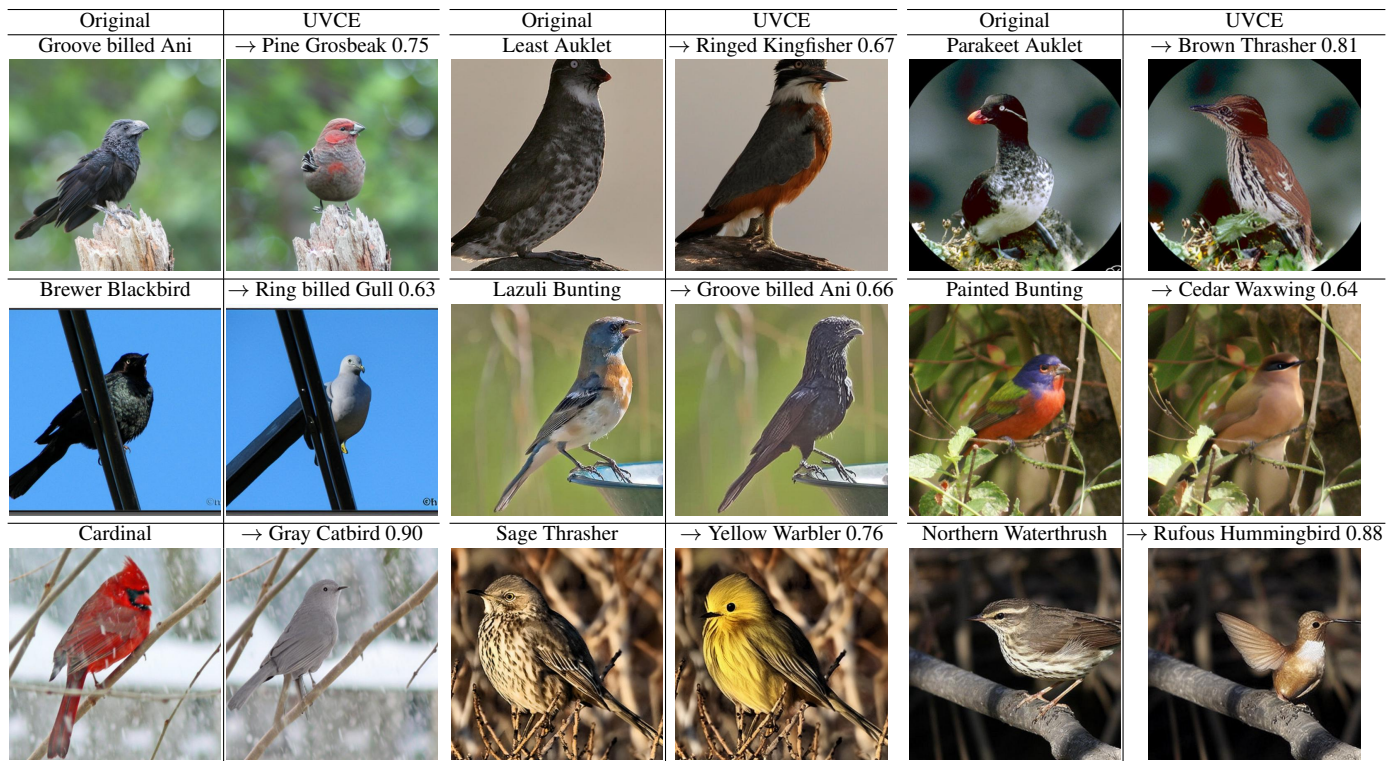


Figure 17. **CUB-200-2011** [81] UVCEs for a ViTMAE [27] pre-trained on ImageNet-1K and fine-tuned on CUB.



Figure 18. **Food-101** [11] UVCEs for a ViT-B/16 AugReg [19, 74] pretrained on ImageNet-21K and fine-tuned on Food-101.



Figure 19. **Stanford Cars** [38] UVCEs for a for a CAL-ResNet101 [55] trained on the Cars dataset.



Figure 20. **FFHQ** UVCEs for a zero-shot attribute classifier based on a CLIPA [41] text and image encoder pair.

D. Classifier Disagreement

In Fig. 21, we extend our analysis of the shape bias of adversarially robust models. In addition to the images from Fig. 3, we also show results from maximizing the standard model while minimizing the robust one. The generated images show a richer texture and the shape differs significantly from the Stable Diffusion initialization which is in line with our findings in Sec. 4. Fig. 22 shows additional results for the zero-shot CLIP where we used a ViT-B as second classifier instead of a ConvNeXt-B. The results show that the choice of the second classifier has only little influence on the detected errors. A reason for this is that the zero-shot model extends the original class to a large set of out-of-distribution images (see Fig. 4) which is not the case for models that were trained or fine-tuned on ImageNet. As described in Sec. 4, we show the results for the different biases of a ViT-B and a ConvNeXt-B in Fig. 23.

D.1. Hyperparameters

Resolution	512
Guidance Scale	3.0
DDIM steps	25
Optimizer	ADAM
Optimization steps	15
C_t, \varnothing_t stepsize	0.025
z_T stepsize	0.00025
Scheduler	cosine
Gradient Clipping	0.05
Num. cutouts	16
Cutout Noise σ	0.05

E. Neuron Activations

We show additional examples for our neuron visualization for the spurious neurons found in [68] and compare to their feature attack (see Fig. 24). Maximizing these neurons starting from images of other classes did not result in a confidence increase as in Fig. 7. Therefore, we cannot confirm that they are also “harmful”.

E.1. Hyperparameters

Resolution	512
Guidance Scale	3.0
DDIM steps	20
Optimizer	ADAM
Optimization steps	20
C_t, \varnothing_t stepsize	0.005
z_T stepsize	0.0005
Scheduler	x
Gradient Clipping	x
Num. cutouts	16
Cutout Noise σ	0.005

F. User Study

For the user study, we collected 30 pairs of original and target class at random and asked 21 participants to answer the four questions described in Sec. 6. All participants are researchers in machine learning or related areas. They participated voluntarily (without payment) and had not seen the generated images before.

During the random selection of examples, we disregarded cases where the optimization failed for one of the methods by thresholding the confidence in the target class at 0.8. We also provided four random training images of the target class as a reference as well as the original image. The VCEs were displayed as “Counterfactual A” and “Counterfactual B” (see Fig. 27). For each participant, the order of the examples, as well as the (per example) assignment of the two methods to “A” and “B” were chosen at random. All images used in the user study can be found in Fig. 25 and Fig. 26.

		p_f : Confidence Robust ViT-S				vs. p_g : Confidence ViT-S		
SD Init.	Head Cabbage (p_f / p_g)		Koala (p_f / p_g)		Brown Bear (p_f / p_g)		Dugong (p_f / p_g)	
	0.57 / 0.95	0.70 / 0.95	0.79 / 0.96	0.76 / 0.97	0.76 / 0.96	0.67 / 0.96	0.01 / 0.01	0.14 / 0.92
								
	0.82 / 0.00	0.79 / 0.00	0.86 / 0.00	0.92 / 0.06	0.80 / 0.00	0.76 / 0.00	0.66 / 0.02	0.78 / 0.00
$p_f \uparrow - p_g \downarrow$								
$p_g \uparrow - p_f \downarrow$	0.00 / 0.96	0.02 / 0.98	0.45 / 0.94	0.06 / 0.96	0.09 / 0.97	0.00 / 0.99	0.06 / 0.96	0.08 / 0.97
								

Figure 21. **Classifier disagreement: shape bias of adversarially robust models (extended)**. This is an extended version Fig. 3 where we additionally show images maximizing the confidence of the standard model and minimizing the confidence of the robust one (third row) while starting from the same initial Stable Diffusion image. In contrast to the second row, these images show significant shape changes and a richer texture compared to the ones of the second row (maximizing/minimizing confidence of the robust/standard model). In particular, the images of the second row are mainly “cartoon”-like versions of the SD initializations with little texture.


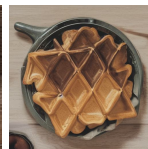


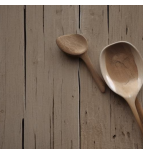
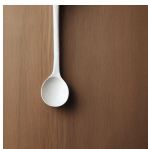
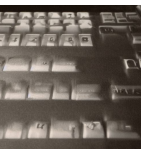


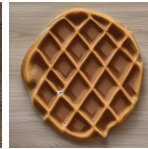


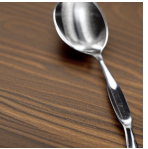


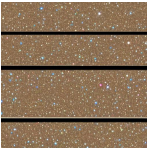

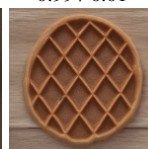
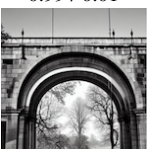


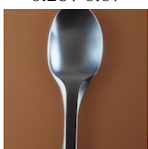

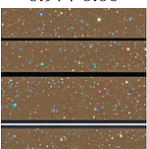
		Waffle Iron (p_f / p_g)		Steel Arch Bridge (p_f / p_g)		Wooden Spoon (p_f / p_g)		Space Bar (p_f / p_g)	
SD Init.		1.00 / 0.51	1.00 / 0.76	0.71 / 0.01	0.86 / 0.00	0.99 / 0.93	0.72 / 0.85	0.09 / 0.01	0.02 / 0.00
									
		p_f : Confidence Zero-shot CLIP ImageNet classifier				vs.	p_g : Confidence ConvNeXt-B		
		1.00 / 0.01	1.00 / 0.00	1.00 / 0.00	1.00 / 0.00	0.98 / 0.00	0.92 / 0.04	1.00 / 0.00	0.99 / 0.00
$p_f \uparrow - p_g \downarrow$									
		p_f : Confidence Zero-shot CLIP ImageNet classifier				vs.	p_g : Confidence ViT-B		
		1.00 / 0.04	0.99 / 0.01	0.99 / 0.01	1.00 / 0.01	0.99 / 0.04	0.26 / 0.07	0.99 / 0.08	0.97 / 0.00
									

Figure 22. **Detected zero-shot CLIP errors are independent of the minimized classifier**: We show the results for maximizing the zero-shot CLIP while minimizing ConvNeXt-B (second row, as in Fig. 5) and minimizing a ViT-B (third row). The zero-shot CLIP extends the original classes to much larger sets of out-of-distributions images compared to models trained or fine-tuned on ImageNet. Therefore, the failure cases discovered by maximizing classifier disagreement do not depend on the choice of the minimized classifier.













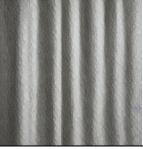












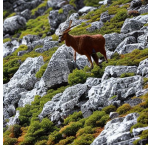










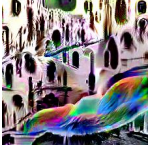



		p_f : Confidence ViT-B vs. p_g : Confidence ConvNeXt-B							
		Goblet (p_f / p_g)		Vase (p_f / p_g)		Shower Curtain (p_f / p_g)		Tabby (p_f / p_g)	
		0.96 / 0.93	0.86 / 0.68	0.83 / 0.76	0.95 / 0.44	0.69 / 0.89	0.99 / 0.92	0.21 / 0.03	0.18 / 0.32
									
		0.99 / 0.81	0.86 / 0.68	0.83 / 0.05	0.96 / 0.04	0.99 / 0.06	0.99 / 0.02	0.88 / 0.05	0.83 / 0.02
	$p_f \uparrow - p_g \downarrow$								
		0.07 / 0.90	0.14 / 0.50	0.18 / 0.89	0.20 / 0.76	0.14 / 0.94	0.07 / 0.96	0.07 / 0.71	0.14 / 0.79
	$p_g \uparrow - p_f \downarrow$								
		0.07 / 0.90	0.14 / 0.50	0.18 / 0.89	0.20 / 0.76	0.14 / 0.94	0.07 / 0.96	0.07 / 0.71	0.14 / 0.79

Figure 23. **Classifier disagreement: ViT vs. ConvNeXt.** For a given class label y , the first row shows the output of Stable Diffusion for “a photograph of y ”. The images in the other rows have been optimized to maximize the difference of the confidence between a ViT-B and a ConvNeXt-B. Empty wine glasses are classified as “goblet” by the ConvNeXt-B, whereas the ViT-B predicts “red wine”. For the class “vase”, realistic images without flower blossoms (high confidence for ViT-B) and paintings with more pronounced blossoms (high confidence for ConvNeXt-B) result in a large difference of confidence. Only the ConvNeXt, but not the ViT, predicts “shower curtain” for colorful exemplars and the opposite holds for the gray ones. A close-up of a cat face with large green eyes triggers only the ViT’s prediction of “tabby cat”, while only the ConvNeXt model assigns a high confidence to a zoomed-out version without eyes.









Neuron 820 (Conf. class Ibex)

[68] Max. Neuron 820	Maximize Neuron 820	← SD → Initialization	Minimize Neuron 820
13.06 (0.18)	3.69 (0.20)	1.06 (0.09)	0.04 (0.01)
			
12.82 (0.45)	2.99 (0.97)	1.48 (0.69)	0.26 (0.02)
			

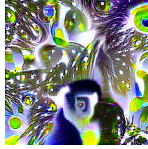
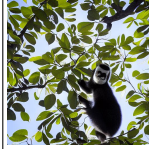
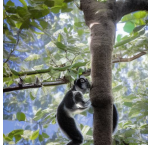
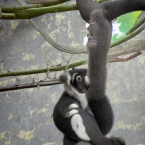
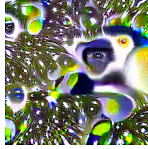
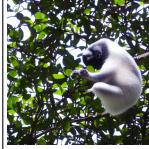

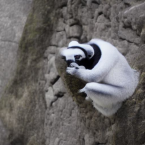
Neuron 481 (Conf. class Gondola)

[68] Max. Neuron 481	Maximize Neuron 481	← SD → Initialization	Minimize Neuron 481
16.01 (1.00)	2.87 (1.00)	1.96 (1.00)	0.16 (0.00)
			
14.07 (0.45)	2.11 (1.00)	0.97 (0.65)	0.12 (0.48)
			




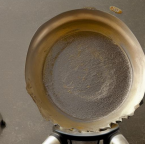




Neuron 1933 (Conf. class Greenhouse)

[68] Max. Neuron 1933	Maximize Neuron 1933	← SD → Initialization	Minimize Neuron 1933
15.15 (0.52)	2.40 (1.00)	0.85 (1.00)	0.02 (0.98)
			
15.07 (0.54)	2.63 (1.00)	0.97 (1.00)	0.10 (0.27)
			

Neuron 1414 (Conf. class Indri)

[68] Max. Neuron 1414	Maximize Neuron 1414	← SD → Initialization	Minimize Neuron 1414
17.00 (0.24)	3.32 (0.47)	0.97 (0.05)	0.28 (0.00)
			
16.33 (0.54)	2.87 (0.67)	1.00 (0.28)	0.01 (0.01)
			

Neuron 2000 (Conf. class Wok)

[68] Max. Neuron 2000	Maximize Neuron 2000	← SD → Initialization	Minimize Neuron 2000
15.11 (0.43)	2.69 (0.89)	0.89 (0.07)	0.01 (0.01)
			
15.14 (0.76)	2.66 (0.80)	0.98 (0.39)	0.12 (0.00)
			

Neuron 1562 (Conf. class Mosquito net)









[68] Max. Neuron 1562	Maximize Neuron 1562	← SD → Initialization	Minimize Neuron 1562
26.51 (0.00)	3.85 (0.94)	0.85 (0.85)	0.01 (0.01)
			
26.42 (0.00)	2.42 (0.62)	0.69 (0.08)	0.03 (0.00)
			

Figure 24. **Additional examples: Neuron visualizations of spurious neurons from [68].** Feature attack [68] and our neuron visualization for the spurious features: “stone/grass” for “ibex” (first row left), “leaves” for “indri” (first row right), “buildings” for “gondola” (second row left), “food” for “wok” (second row right), “flowers” for “greenhouse” (left) and “bed” for “mosquito net” (third row right).

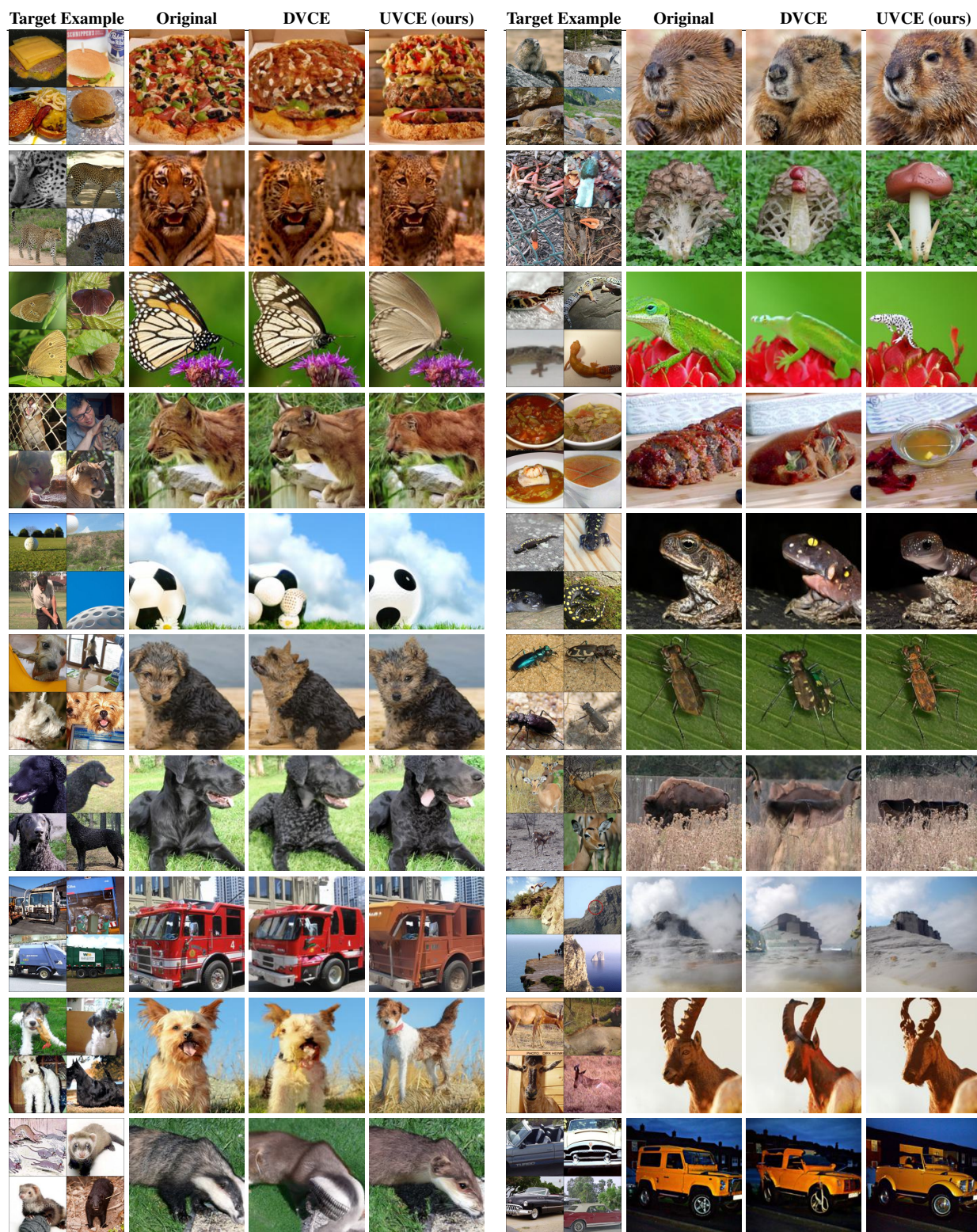


Figure 25. **User Study:** Examples 1-20

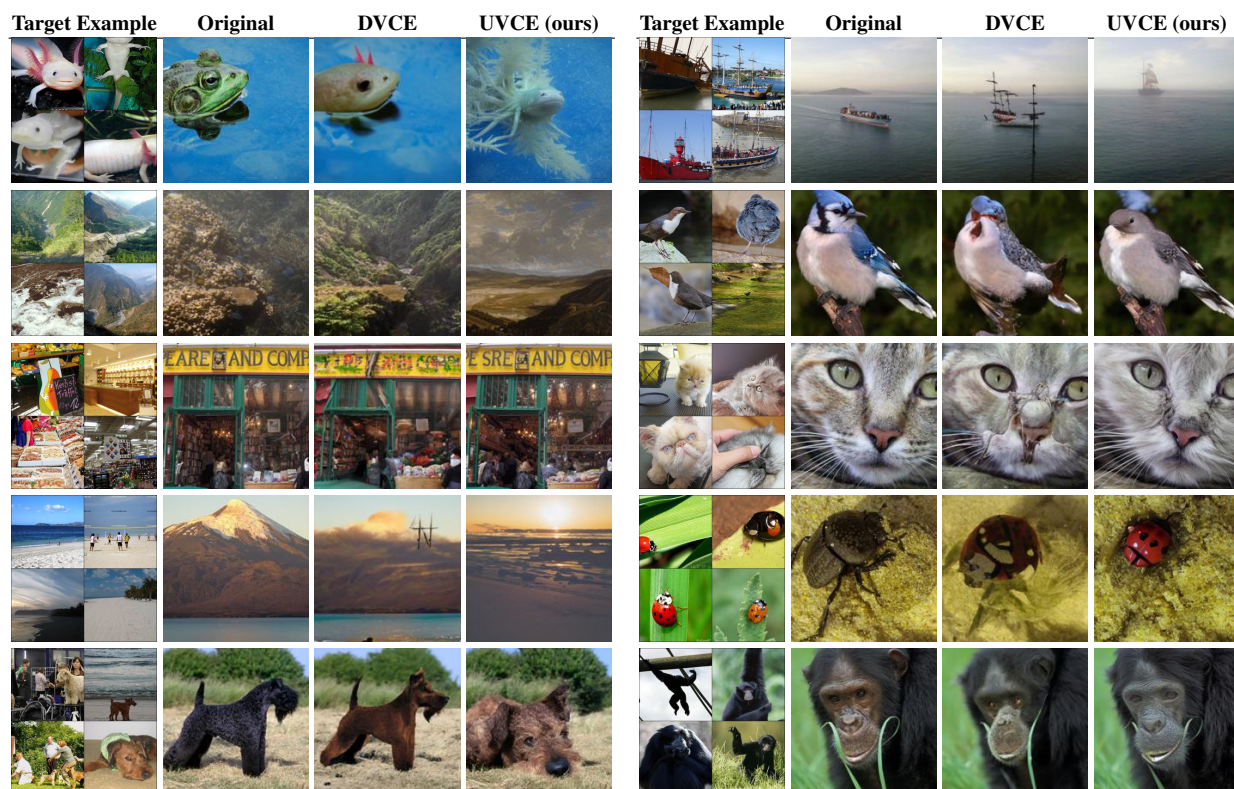


Figure 26. **User Study:** Examples 21-30

Target Example: ringlet

Original: monarch

Counterfactual A: to ringlet

Counterfactual B: to ringlet

The counterfactual image ...

... is realistic.

... shows meaningful features of the target class.

... changes mainly the class object.

Which counterfactual is better?

Counterfactual A

Counterfactual B

Yes No

Yes No

Yes No

Yes No

Counterfactual A Equal Counterfactual B

Image Size

Previous

Next

Figure 27. **User Study:** The participants were shown four training images of the target class, the original image and the two VCEs.